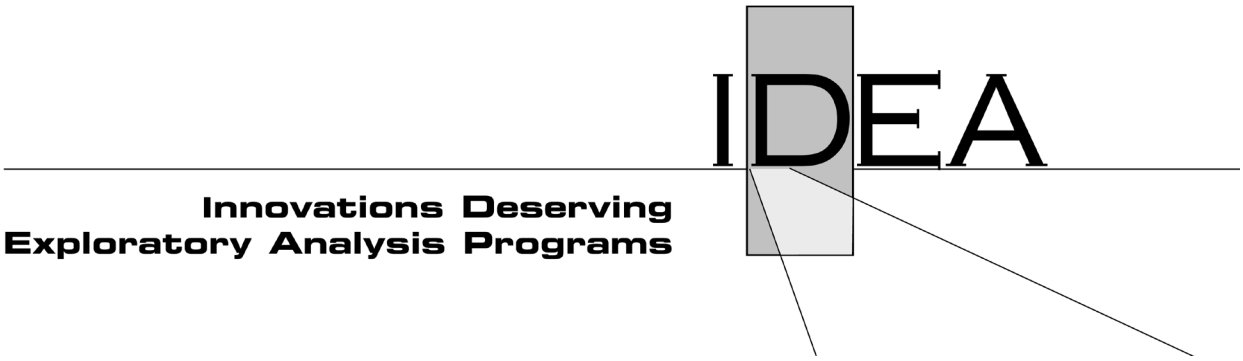


***Rail Safety IDEA Program***

# Laser-Based Non-destructive Spike Defect Inspection System

Final Report for
Rail Safety IDEA Project 44

Prepared by:
Yu Qian
Dimitris Rizos
Robert Mullen
University of South Carolina

***July 2022***

NATIONAL ACADEMIES Sciences Engineering Medicine

TRB TRANSPORTATION RESEARCH BOARD

## Innovations Deserving Exploratory Analysis (IDEA) Programs Managed by the Transportation Research Board

This IDEA project was funded by the Rail Safety IDEA Program.

The TRB currently manages the following three IDEA programs:

- The NCHRP IDEA Program, which focuses on advances in the design, construction, and maintenance of highway systems, is funded by American Association of State Highway and Transportation Officials (AASHTO) as part of the National Cooperative Highway Research Program (NCHRP).
- The Rail Safety IDEA Program currently focuses on innovative approaches for improving railroad safety or performance. The program is currently funded by the Federal Railroad Administration (FRA). The program was previously jointly funded by the Federal Motor Carrier Safety Administration (FMCSA) and the FRA.
- The Transit IDEA Program, which supports development and testing of innovative concepts and methods for advancing transit practice, is funded by the Federal Transit Administration (FTA) as part of the Transit Cooperative Research Program (TCRP).

Management of the three IDEA programs is coordinated to promote the development and testing of innovative concepts, methods, and technologies.

For information on the IDEA programs, check the IDEA website (www.trb.org/idea). For questions, contact the IDEA programs office by telephone at (202) 334-3310.

IDEA Programs
Transportation Research Board
500 Fifth Street, NW
Washington, DC 20001

# Laser-Based Non-destructive Spike Defect Inspection System

## IDEA Program Final Report

**Reporting Period:**
11/17/2020 – 5/30/2022

**Rail Safety IDEA Project RS-44**

IDEA Program
Transportation Research Board
National Academies of Sciences, Engineering, and Medicine

Yu Qian, Dimitris Rizos, Robert Mullen
University of South Carolina

7/15/2022

# TABLE OF CONTENTS

## Executive Summary

Spikes, together with tie plates and timber ties, are the dominant track components in North American freight railroads. For centuries, spikes, with marginal changes in terms of geometry and material, have consistently provided reliable restrictions to rails. With the varying axle load and operational speed, spikes are subjected to more demanding loading conditions, especially in the territories where tracks have high curvature and anchors are replaced with elastic fasteners. Recent inspections have identified frequent broken spikes in certain tracks. Traditional track inspection methods can hardly identify any broken spikes without manually pulling each spike out, of which is impractical. This IDEA project aims to develop a low-cost, non-destructive and contact-free intelligent inspection system, that is field-deployable on a geometry car, high-rail vehicle, or other type of track inspection platform to identify broken spikes in real-time.

Previous research efforts conducted by the University of Illinois and the Transportation Technology Center, Inc., have greatly improved the understanding of the cause of broken spikes and the potential of using contact-type ultrasonic sensors to detect broken spikes in the field. This project first conducted numerical simulations to test the concept of using a laser to excite the spikes and estimate the reflection signals to distinguish broken spikes and good spikes.

With the guidance of the numerical simulation results, laboratory experiments were also performed using laser pulses to excite the spike head and using a microphone and air coupled transducer to detect the reflection wave signals. The effect of different laser intensities and focus areas were investigated. Due to the high reflection rate of the spike's head surface, a limited amount of laser energy penetrated into the spike. An ordinary microphone was not able to record distinguishable signals from the reflection waves from different spikes, even when the laser energy intensity was high enough to cause safety concerns. Fortunately, with guided wave and air-coupled transducer (ACT), the limited reflection wave could be detected and analyzed. Experiments with spikes oriented in both horizontal and vertical directions were performed. With a carefully tuned setup in the laboratory, it was possible to distinguish broken spikes from good spikes.

The specific accomplishments of this project include:

- Parametric analysis through finite element modeling to investigate the reflection signals with different laser intensities, focus areas, and exposure shapes.
- Laboratory testing of different spikes with laser pulses and microphone.
- Laboratory testing of different spikes with laser optical sensor and air-coupled transducer.
- Safety evaluation of using a laser to excite spikes in the laboratory.
- Development of an automatic real-time spike recognition and segmentation algorithm

## IDEA Product

### I. FEM Heat Transfer and Wave Propagation Model for Spike

A numerical model of a spike based on the finite element method was established to simulate the heat transfer from laser excitation and corresponding thermal expansion and wave propagation within the spike. Three different types of spikes, good spike (new spike with no crack), partially cracked spike, and completely broken spike (hereafter referred to as broken spike), are included in the model. Laser excitation was simulated as a heat source at the spike head area to mimic different laser exposure times and focus areas. The wave caused by the laser excitation at the spike head area can be reproduced by the numerical model to present the wave initiation and propagation within the spike. The numerical model can be used to perform a parametric analysis to guide potential laboratory setups to use the appropriate energy density.

### II. Laser Based Broken Spike Detection

A series of laboratory experiments were performed with the guidance from the numerical simulation results. Different spikes were excited with a laser directly hit at the spike head at different laser intensities. Both a microphone and air-coupled transducer were used to detect the reflection waves away from the spike in a non-contact fashion to distinguish any difference that may show between the signals from good spikes and broken spikes. The specific laboratory setup with the air-coupled transducer developed in this project could pick up the differences between the signals from good spikes and broken spikes.

### III. Automatic Spike Detection Algorithm

A real-time pixel-level detection framework with improved real-time instance segmentation models was developed based on a fully convolutional model including backbone, FPN, Protonet, and prediction head. The developed algorithm leverages fast object detection and highly accurate instance segmentation. Backbones with more granular levels and receptive fields are implemented in the proposed models. Track components such as spike, clip, and rail can be detected in real-time (inference speed over 30 FPS) with a single GPU. Under the different light conditions, our proposed models outperform other models, proving the robustness on low visibility conditions.

## Concept and Innovation

Although many new types of elastic fasteners and concrete ties have been recently introduced, spikes, together with tie plates, are still one the major fastening systems in North American freight railroads. For centuries, spikes, with marginal changes in terms of geometry, have consistently provided reliable restraint to tie plates and rails in vertical direction. Spikes are used to fix tie plates to the timber, or composite ties when elastic fasteners are used to restrain the rail. With the increasing axle load and operational speed, spikes are subjected to more demanding loading conditions, especially in the territories where tracks have high curvature (Dersch et al. 2019, Roadcap et al, 2019, Trizotto et al. 2019, Dersch et al. 2020). It is reported that broken spikes were frequently observed, including cut spikes, screw spikes, and driven spikes that were used to restrict both tie plates and rails (Gao et al. 2018, Roadcap et al, 2019). Since cracks typically develop between one and two inches below the top of the tie, it is very difficult to distinguish the broken spikes without physical examination, which causes formidable challenges in track health evaluation and operational safety (Gao et al. 2018, Roadcap et al, 2019). Roadcap (2019) reported that one railroader acknowledged the broken spike was the greatest problem for the track they owned. Several recent derailments in Canada and the United States are attributed to a large number of broken spikes or screws within a certain section of track (Kerchof 2017). A recent investigation conducted by Roadcap et al. (2019) identified at least 11 derailments were due to the broken spikes.

Traditional track inspection methods cannot identify broken spikes other than manually pulling each spike out or tapping the spike heads and listening (Roadcap et al 2019), thus impractical. To understand the underlying failure mechanisms and to develop preventive strategies for the spike failures, previous research has primarily focused on the force distribution, force transmission, and damage development mechanisms at track, tie, and individual spike levels by numerical simulations (Stuart et al., 2019 and 2020; Dersch et al., 2019, 2020, 2021a and 2021b; Yu and Liu, 2019). Recently, Transportation Technology Center Inc. (TTCI) and the University of Illinois began to examine the spikes with instrumented strain gages to sense the load (Gao et al., 2020, Dersch et al. 2021a and 2021b). The Federal Railroad Administration (FRA) and TTCI have completed a preliminary investigation of ultrasonic techniques to identify cracked or broken spikes in tracks (Gao et al., 2021). The ultrasonic piezoelectric transducer has shown some degree of success in detecting the broken spikes. However, as the report mentioned, using those types of piezoelectric transducers in the field is still challenging. The results are sensitive to how hard the inspector presses the sensor against the spike head, especially when the spike head is not smooth.

Considering the enormous number (estimated around two billion) of spikes in service, the drastic consequences of unrecognized broken spikes, and the challenge to quantify the service condition of the spikes, the objective of this project is to develop a non-destructive and contact-free intelligent inspection system that can be deployed for track inspections. We propose to develop the laser-based, non-destructive spike defect inspection system based on laser excitation, acoustic analysis, computer vision and pattern recognition, and artificial intelligence (AI). A laser will be used to excite the spike head by introducing sufficient energy within the focused area over a short period of time. The absorbed energy will introduce a heated area at the spike head and cause corresponding thermal expansion, generating a mechanical wave. The wave will propagate through the spike shaft and reflect from the bottom of the spike or other interfaces of any internal cracks or defects. The reflected

wave may generate an acoustic signal that may be capable of detection by a microphone, air-coupled transducer, or other type of sensors. It is hypothesized that spikes with and without a crack will generate different signals due to different wave propagation paths. Thus, it will be possible to distinguish a broken spike from good spikes through a non-contact fashion.

Preliminary experiments indicate that if using an ordinary microphone, the laser needs to have high power; however, it may cause laser scattering issues due to the high reflective properties of the spike head surface. With an ultrasonic guided wave and air-coupled transducer, it can distinguish the broken spike from good spike in the laboratory setup.

To identify the spikes on a track, a fast algorithm that is able to detect the spikes in real-time is needed. This study has developed a real-time instance segmentation model and tailored it for the application on the railroad track component detection. This model is developed based on a fully convolutional model, and experimental results show our proposed models outperform the state-of-the-art models on detection accuracy.

## Investigation

There were two major steps of this project during Stage I: 1) Parametric analysis through numerical simulations and 2) Laboratory experiments with non-contact excitation including one major step during Stage II: automatic real-time spike recognition and segmentation. The specific work performed during this project is described below:

### 1 Numerical Parametric Analysis

***Model setup***

Numerical simulations were performed based on the finite element method with Abaqus to analyze the possible heat transfer and wave propagation when a temperature jump is induced by a laser on the spike head. The spike was simulated to the geometry of a typical cut spike as described in the AREMA manual (AREMA 2014). The element used for the spike was C3D8T, 8-node thermally coupled brick, trilinear displacement, and temperature. The material properties are typical steel material properties, including the thermal conductivity of 45 W/mK, density of 7,800 kg/m$^3$, modulus of elasticity of 205 GPa, thermal expansion coefficient of 1e-5, and the specific head of 490 kg/J/C. The initial trial laser pulse width was set as $t_r = 1.0 \times 10^{-6}$ s $= 1.0$ μs and $t_{\text{sim}} = 1.0 \times 10^{-4}$ s $= 100$ μs. The focus area was set as $A = 4.0 \times 10^{-6}$ m$^2$. The power per Area was $q = 5.0 \times 10^{11}$ J/(m$^2 \cdot$ s) , and the power per pulse was $2.0 \times 10^6$ W, which can be calculated as power per area multiplied by the focus area. Because this project was more interested in the wave propagation within the spike instead of the heat absorption, the reflection was not considered in the simulation. The heat introduced by the laser is simplified to be a surface heat flux at the spike head instead of a light source. The dynamic temperature-displacement simulation time was 5e-5 sec. Figure 1 provides the overview of the spike model and the decaying amplitude for each pulse.

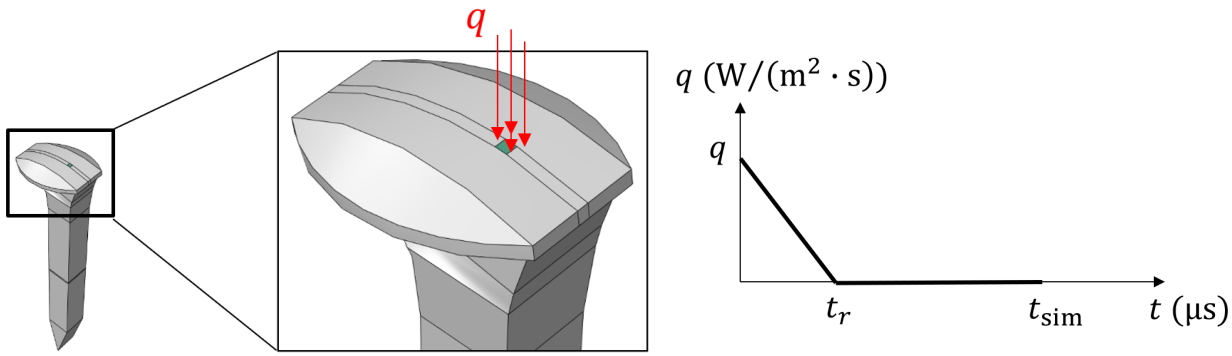


(a) 3-D spike model (b) Decay amplitude of each pulse

Figure 1. Overview of the spike model in simulation

To investigate the different responses from different spikes, three spikes were included, a good spike (without any defect), a partially cracked spike (50% cracked at the middle of the spike shaft), and a broken spike (100% cracked at the middle of the spike shaft). To investigate the effect of power per pulse, three different values of the power per pulse were included, $2.0 \times 10^6$ W, $4.0 \times 10^6$ W, and $8.0 \times 10^6$ W. Figure 2 presents an example of the typical results of wave initiation and propagation in the spike. The heated area would expand due to the temperature jump, and the expansion created

a wave propagating towards the rest of the head and the bottom of the spike. The blue color in Figure 2 is the area that the wave has not yet reached. The warmer colors indicate the magnitude of displacement due the wave propagation, with a more reddish color indicating higher displacement and the more greenish color indicating lower displacement.

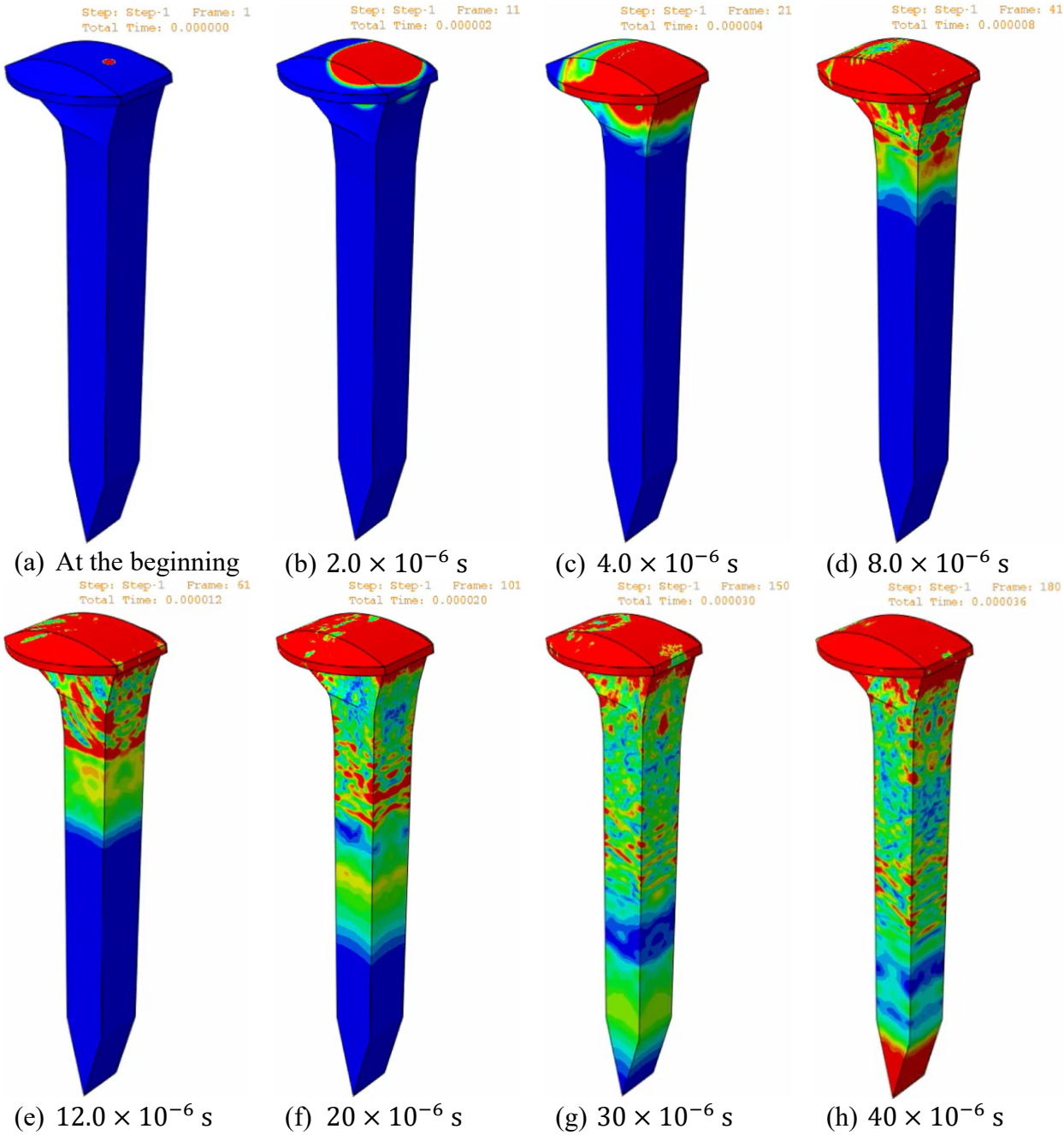


(a) At the beginning (b) $2.0 \times 10^{-6}$ s (c) $4.0 \times 10^{-6}$ s (d) $8.0 \times 10^{-6}$ s

(e) $12.0 \times 10^{-6}$ s (f) $20 \times 10^{-6}$ s (g) $30 \times 10^{-6}$ s (h) $40 \times 10^{-6}$ s

Figure 2. Example of the wave initiation and propagation process

It is hard to conclude anything from a single simulation other than to confirm the potential of wave propagation in the spike due to a surface heat flux, which can be generated by laser. To distinguish

a broken spike from a good spike, the wave propagation needs to present noticeable differences. Figure 3 shows the comparison of the wave propagation in different spikes when subjected to the same surface heat flux. Similar as Figure 1, for a good spike with no crack, the wave can smoothly propagate towards the bottom of the spike. However, the wave cannot pass through any cracks due to the discontinuity. For the partially cracked spike, the wave can only propagate along where the crack has not yet reached. For the broken spike, the wave is reflected at the interface. Essentially, the broken spike was a spike having a shorter shaft. Due to the differences in wave propagation at different spikes, the reflection wave would travel different distances until it came back to the spike head. Thus, the displacement at the spike head may show different magnitudes which may also produce different acoustic signals.

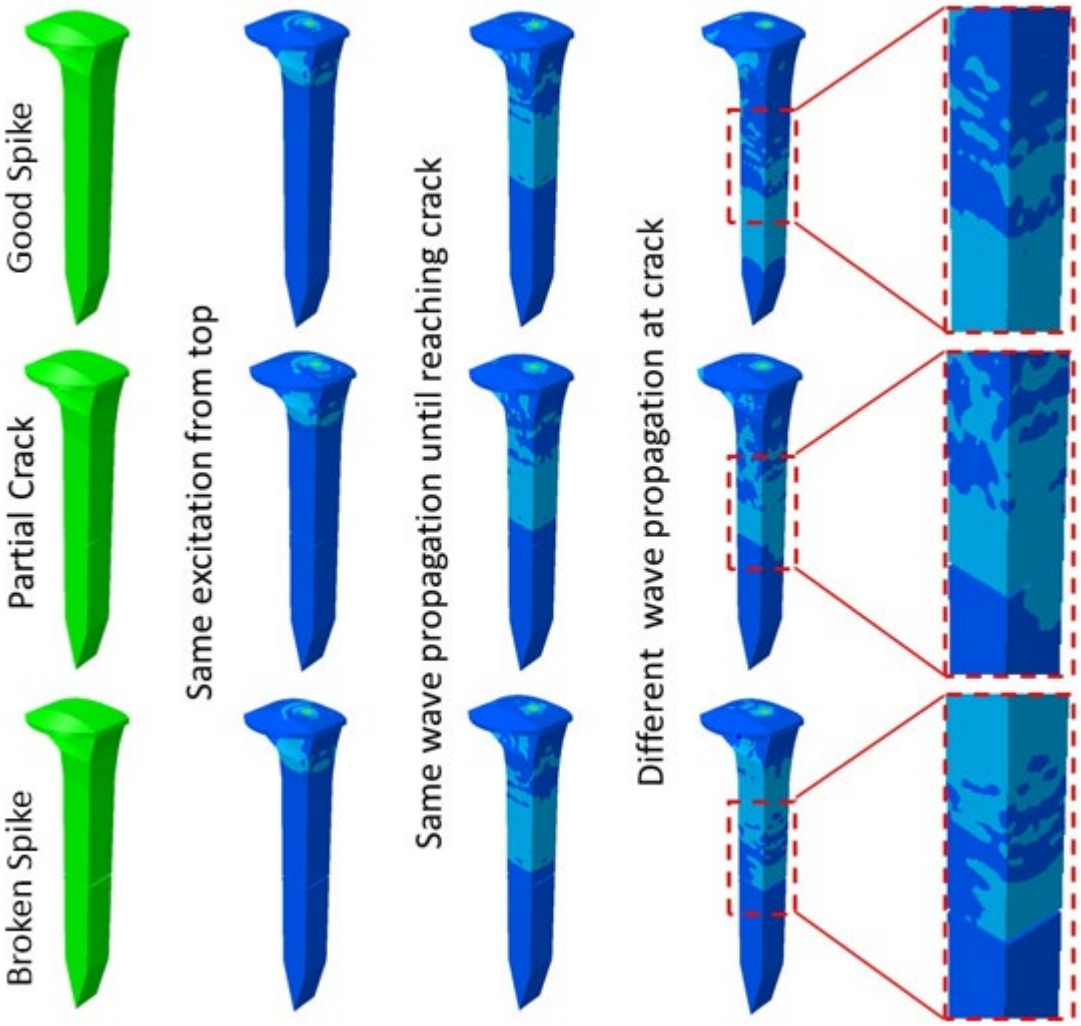


Figure 3. Example of the wave propagation in different spikes

***Effect of laser focus area***

Figure 4 shows the different laser focus areas, and Figure 5 shows the results of the spike head displacement when different spikes were subjected to the same excitations. This displacement is initiated from the spike head. The small, heated area at the spike head expands due to the increased

temperature introduced by the laser pulse. With the power per pulse of $2.0 \times 10^6$ W and focus area of $4.0 \times 10^{-6}$ m$^2$, little difference can be observed as shown in Figure 4 (a). When the focus area was reduced to $1.0 \times 10^{-6}$ m$^2$, slight difference can be observed in Figure 4 (b). With the same power per pulse, the differences of the spike head displacement were more pronounced if the focus area reduced $2.5 \times 10^{-7}$ m$^2$. Figure 5 suggests the laser excitation to spike head should have sufficient energy density, otherwise, there would not be any distinguishable signals. Note the differences presented in Figure 5 is small, which may be hard for the sensors to detect.

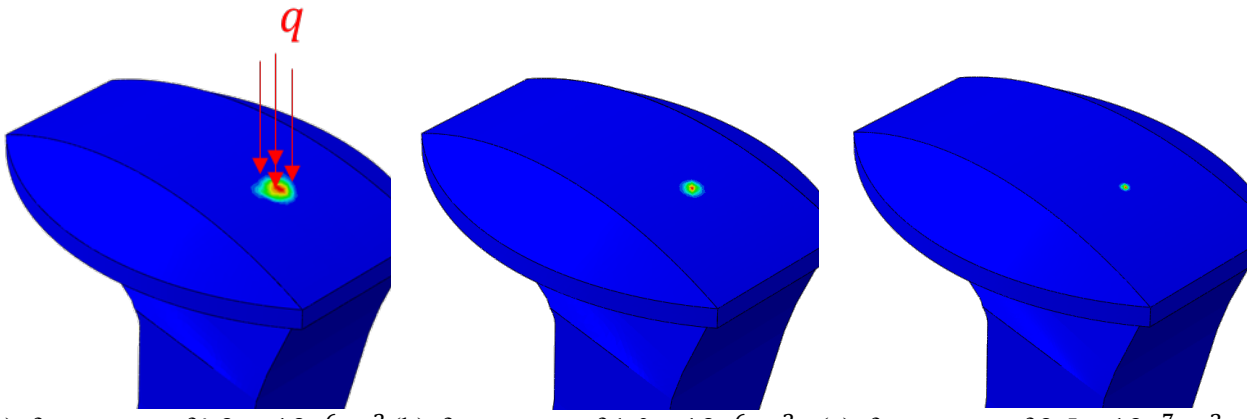


(a) focus area of $4.0 \times 10^{-6}$ m$^2$ (b) focus area of $1.0 \times 10^{-6}$ m$^2$ (c) focus area of $2.5 \times 10^{-7}$ m$^2$

Figure 4. Example of the effect of laser focus area

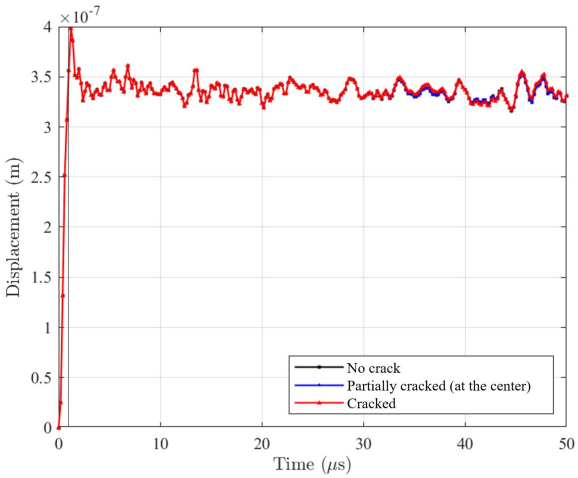


(a) focus area of $4.0 \times 10^{-6}$ m$^2$

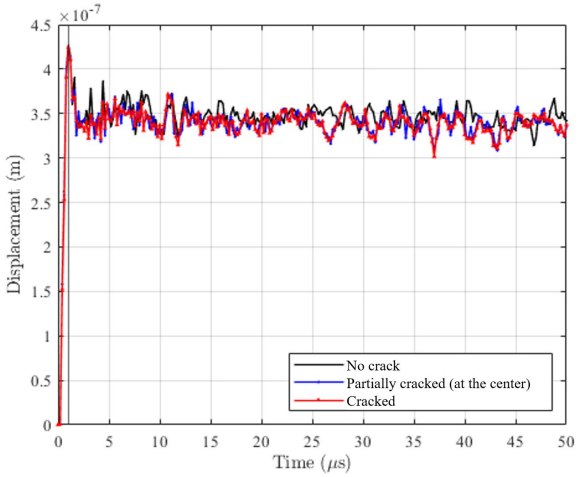


(b) focus area of $1.0 \times 10^{-6}$ m$^2$

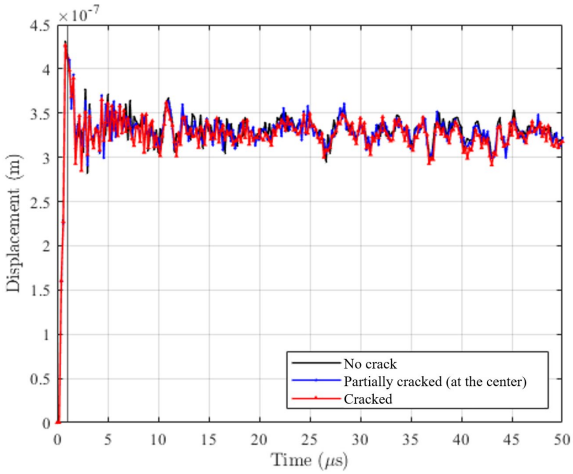


(c) focus area of $2.5\times 10^{-7}$ $m^2$

Figure 5. Spike head displacement with different laser focus area

***Effect of laser focus shape***

Due to the geometric differences between the spike head and shaft, there could be a boundary effect at the connection when the waves propagate from the spike head to the shaft, which can be seen from Figure 2 (c) and (d). One possible reason was the small focus area at the center of the spike head that caused the wave to propagate not only towards the bottom of the spike, but also towards the boundary of the spike head. Thus, extra simulations were performed to change the focus area from a circle to a strip to reduce the boundary effect. Figure 6 illustrates the simulations with a focus area of a strip instead of a circle.

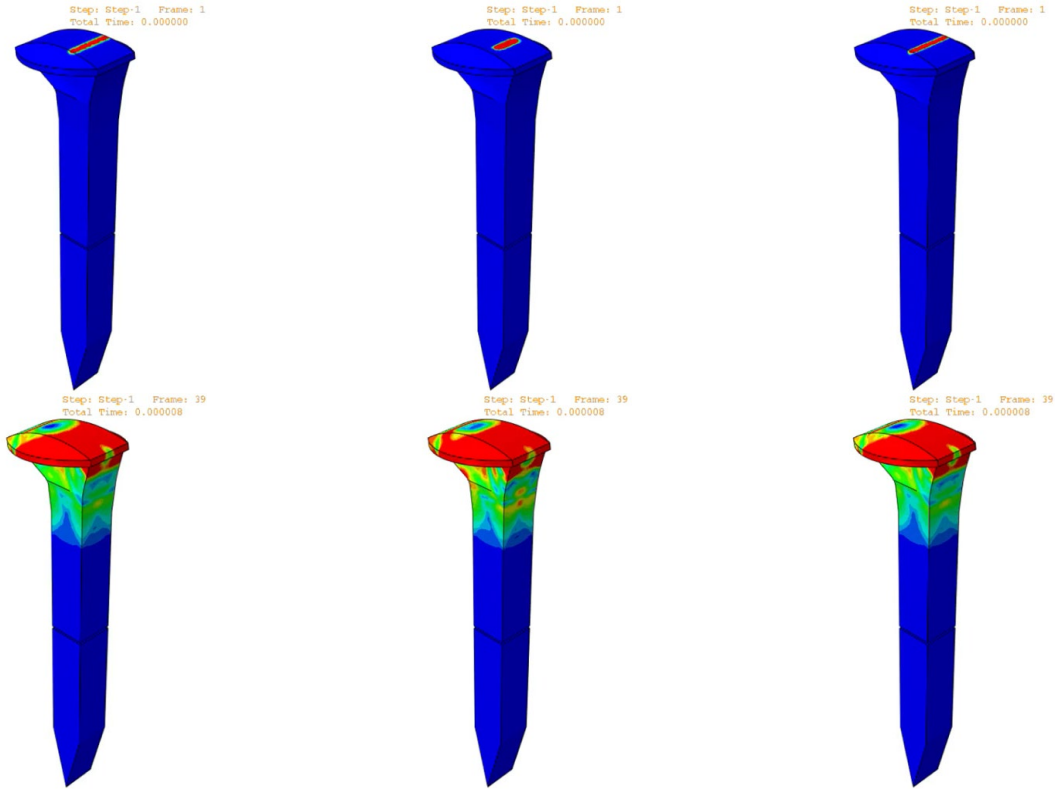

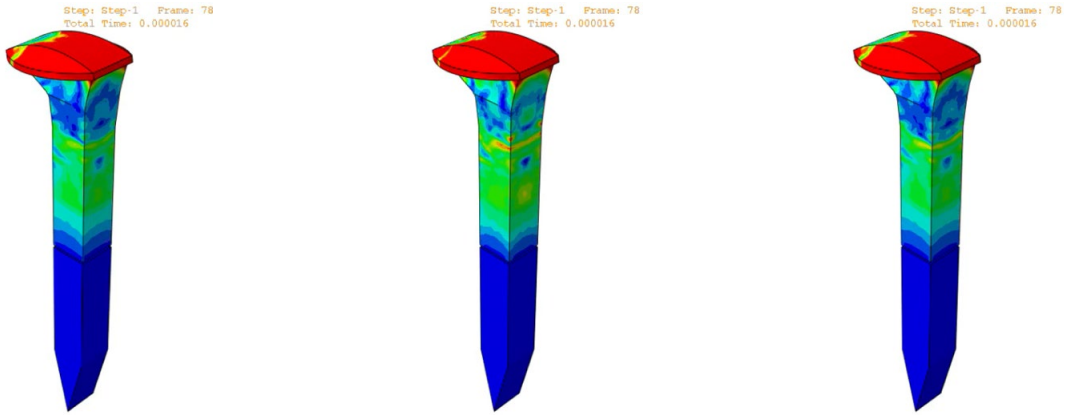

(a) focus area of $3.6 \times 10^{-5}$ m$^2$ (b) focus area of $1.8 \times 10^{-5}$ m$^2$ (half width) (c) focus area of $1.8 \times 10^{-5}$ m$^2$ (half length)

Figure 6. Simulations with a strip shape focus area on a cracked spike

***Effect of laser power per pulse***

Other than changing the focus area, another parameter that might influence results was the power per pulse. Because the differences in displacement were relatively small, higher power per pulse were simulated with the same focus area of $3.6 \times 10^{-5}$ m$^2$; the results are presented in Figure 7. It can be observed that the difference between the good spike and cracked spike was obvious, but the differences between the power levels adopted in the simulations here were very marginal.

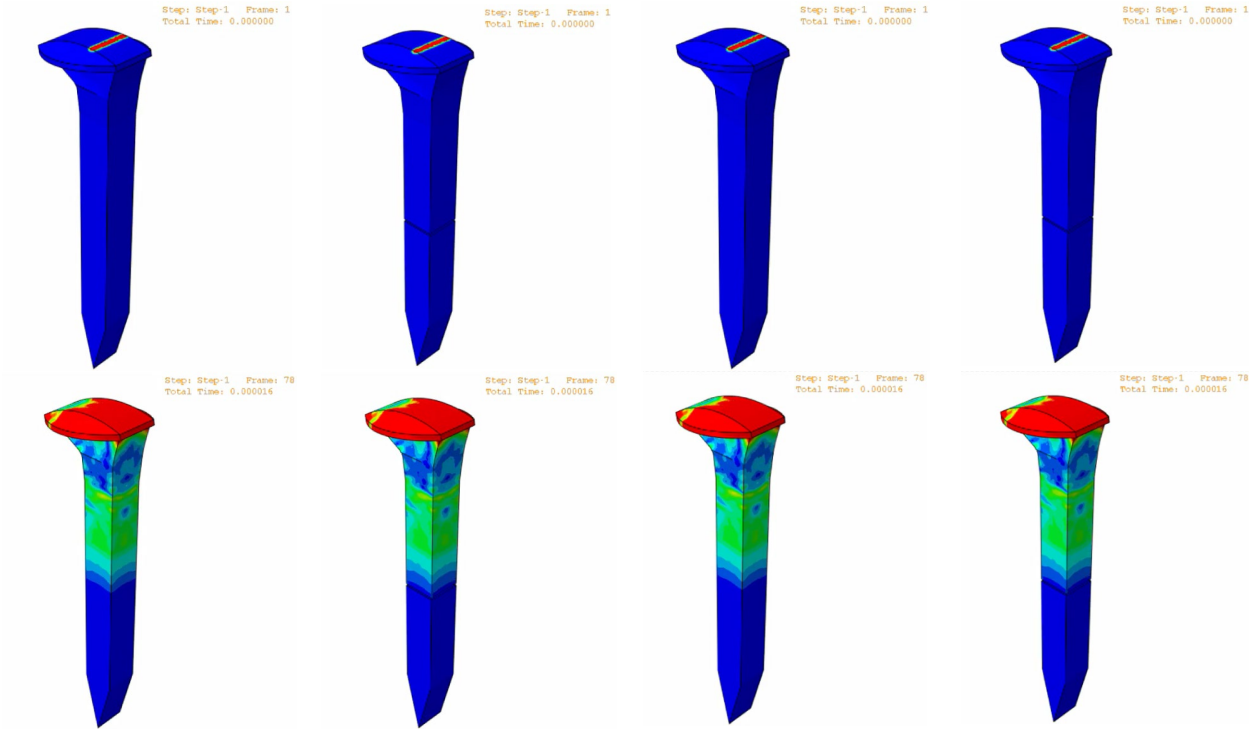

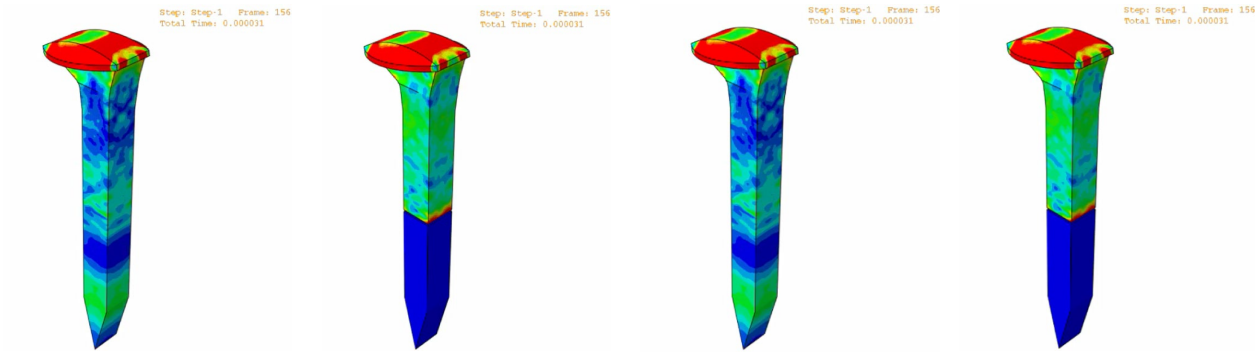

No crack Cracked No crack Cracked

(a) power per pulse $2.0 \times 10^6$ W (b) power per pulse $4.0 \times 10^6$ W

Figure 7. Simulations with different power per pulse

Based on the simulation results, it is possible that under laser excitations, good spikes and cracked spikes will have different spike head displacement leading to different acoustic signals. The difference between the different signals may be able to be measured by suitable sensors. The following section will discuss the effort to measure the difference in the acoustic signals in the laboratory.

## 2. Laboratory Experiments with Laser

***Experiment with pulsed laser and microphone***

The numerical simulations indicated different spikes would produce different displacements at the spike head. The differences of spike head displacement were likely to introduce distinguishable acoustic signals. According to Setiawan et al. (2018), it may be possible to detect the different acoustic signals with ordinary microphones. Thus, the initial laboratory setup was prepared to use an ordinary microphone to "listen" to the acoustic signals from the spike under laser excitation; Figure 8 shows the initial laboratory setup. Note the laser device and the accessories were supported as a courtesy by Dr. Jun Liu's laboratory in the Department of Mechanical and Aerospace Engineering at North Carolina State University. The spike was excited with a Spectra-Physics brand ultrafast laser produced by MKS Instruments, Inc. The light wavelength was 780 nm, the repetition rate was 80 MHz, and the averaged power was 20 mW. The focus was set to a spot with the size of 10 micro, although the spot at the spike head shown in Figure 8 appears to be bigger. The microphone used in the laboratory was a Rode brand NT5 compact 1/2" cardioid condenser microphone. This microphone was designed to collect sounds within a frequency range between 20Hz and 20kHz, a sensitivity of -38.0dB re 1 Volt/Pascal (12.00mV @ 94 dB SPL) +/- 2 dB @ 1kHz, and the maximum sound pressure limit was 143dB.

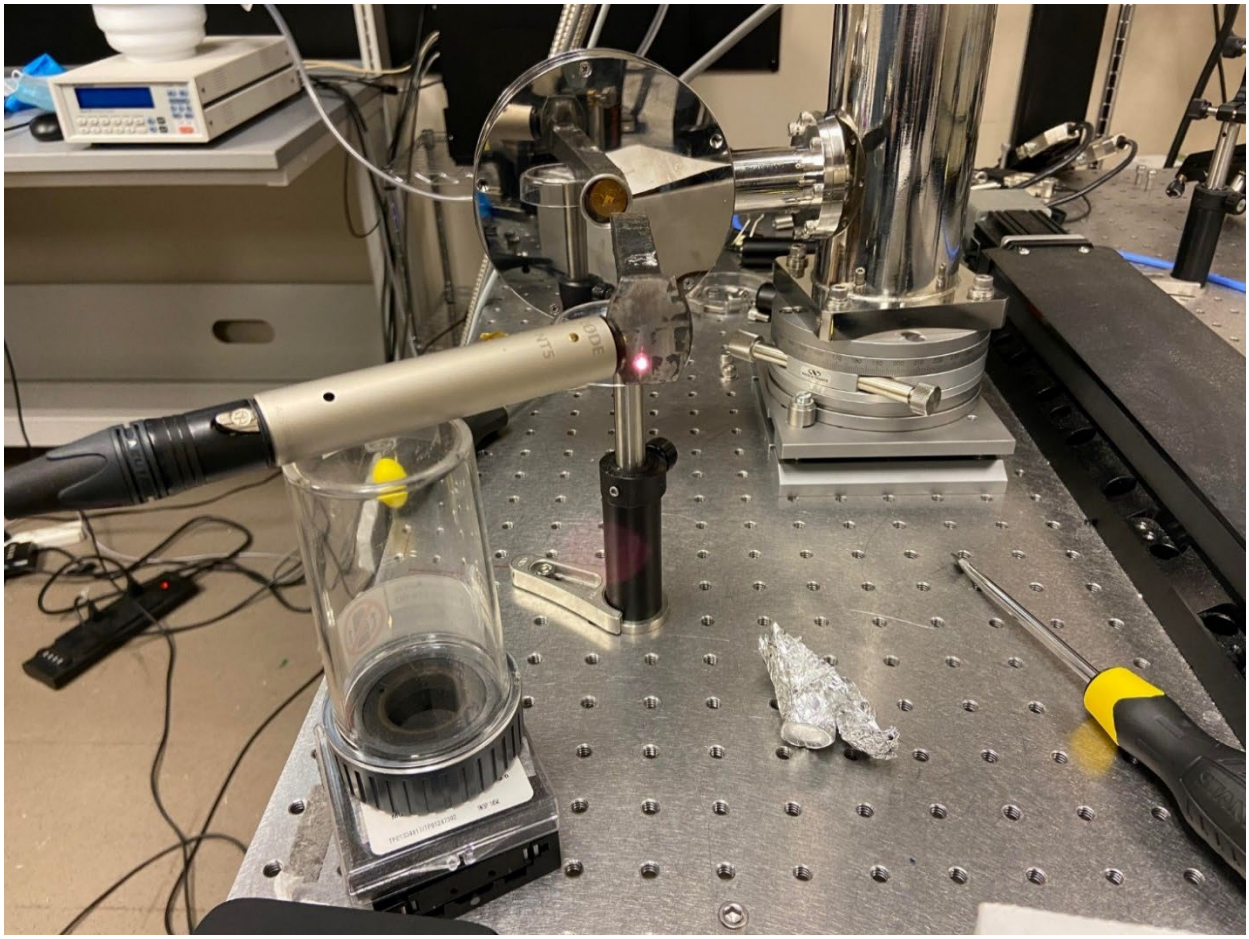

Figure 8. *Laboratory* Setup with laser and microphone at NCSU

Unfortunately, under laser excitation, the microphone did not present any meaningful signals. When increasing the laser power, the signal from the microphone did not show any noticeable changes. On the other hand, when the power level was increased, the laser scattering issue became more pronounced, which was dangerous to continue to increase the power level. An alternative method is to excite the spike with a different type of excitation other than laser. Figure 9 compares the signals picked up by the microphone from the spike under laser excitation, human vocal signals, and the from the spike under excitation by a hammer. It is clear the issue was the energy transferring rate was too low. The possible reason of the failure of this round of testing is the surface reflection of the spike head. During the simulation, it was assumed a heat flux could penetrate into the spike head, while in the laboratory experiment, the spike head was exposed directly to laser instead of a heat flux. The metal material could cause a large portion of reflection of laser instead of effectively absorbing the light energy and transferring that into heat. According to the literature (Kunz and Wegener 2010), the refection of steel or iron was around 65%. Thus, a safe solution would be either looking for a better sensor or increasing the energy transfer rate during the experiment.

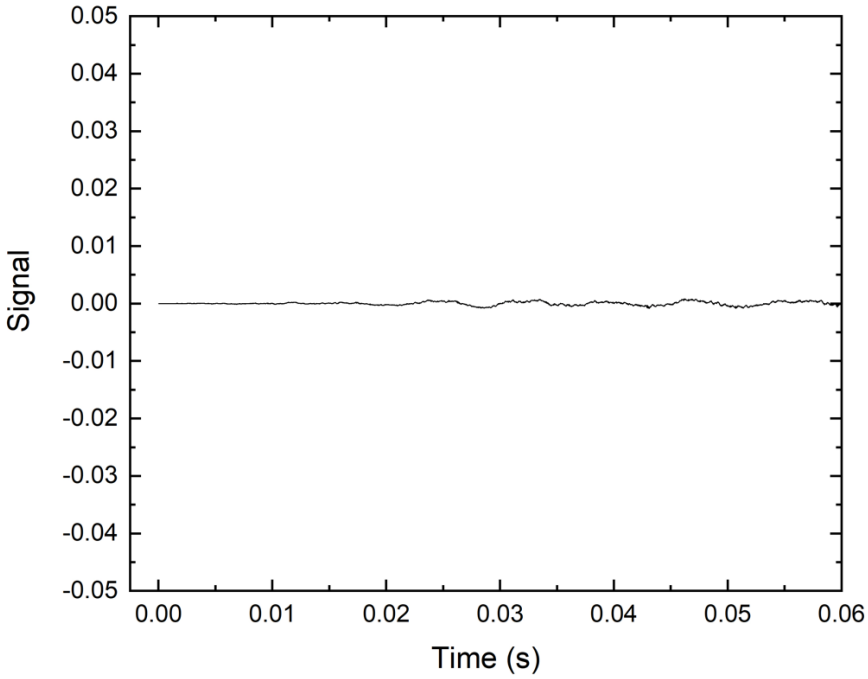


(a) Laser irradiation

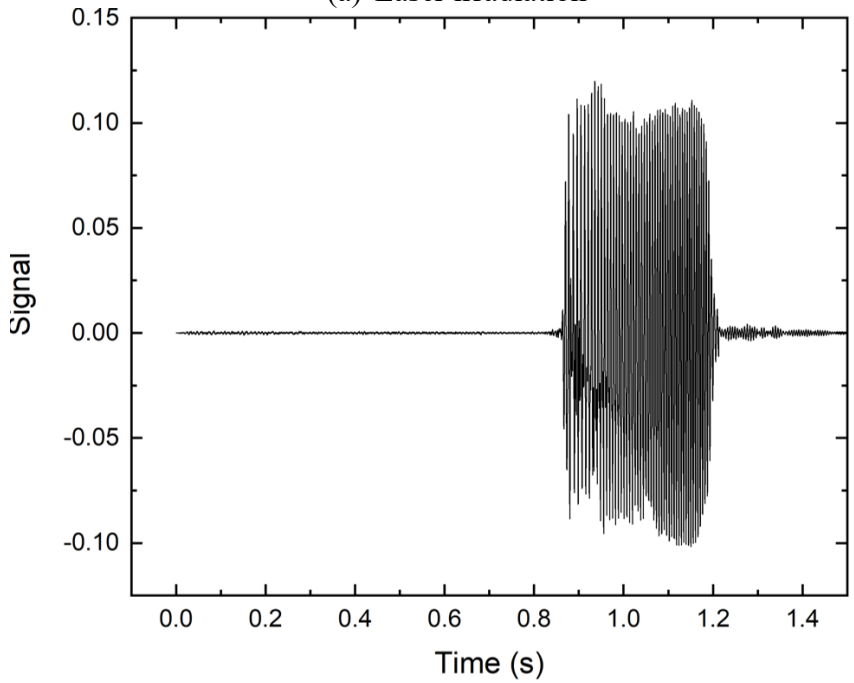


(b) Human vocal

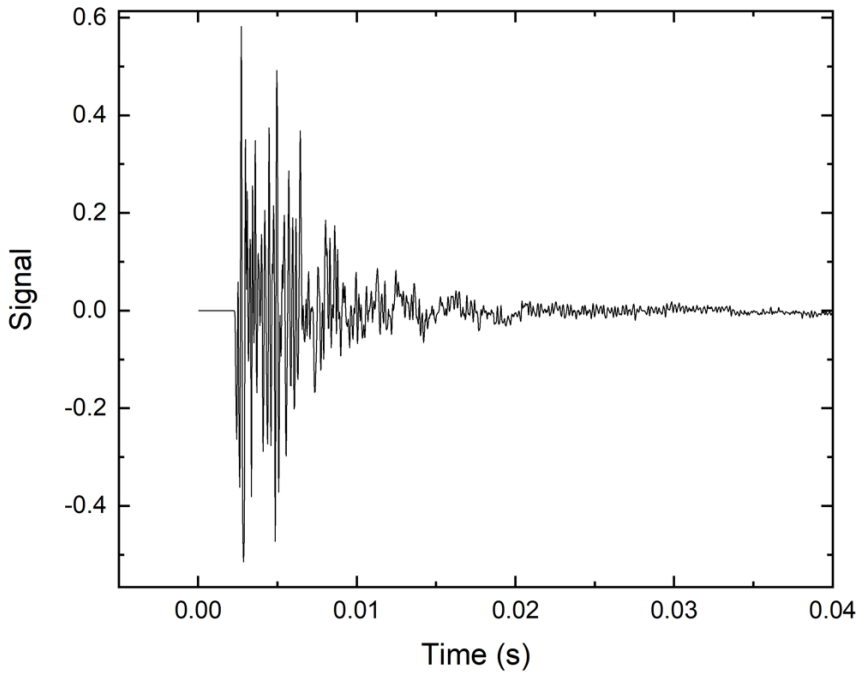

(c) Hammer excitation

Figure 9. Example signals picked by different excitations from setup at NCSU

***Experiment with guided wave and air-coupled transducer***

Inspired by the recent success of a fully, non-contact NDI system, utilizing a low-frequency ultrasonic guided wave concept for imaging barely visible impact damage (BVID) in aerospace composite structures in the literature (Harb and Yuan 2018), the research team worked on using a guided wave and air-coupled transducer (ACT) to search for possible solutions. The air-coupled transducer used in this study was an Ultran brand NCT2-D13 type air coupled transducer. This point (spherical) focused transducer had a 13mm active diameter and a nominal frequency of 2 MHz. Figure 10 shows the laboratory setup of the experiment with the air-coupled transducer. Note that other than the air-coupled transducer, the laser device and accessories were supported as a courtesy by Dr. Fuh-Gwo Yuan's laboratory at the National Institute of Aerospace (NIA). The experiment was also assisted by Dr. Yuan's students at NIA as a courtesy. After a trial-and-error process, the NCT2-D13 ACT was changed to an Ultran NCG100-D25-P76 air-coupled transducer with a diameter of 1 in., a focus of 3 in., and an operating frequency of 100 kHz was used with a 3-peaked toneburst excitation signal. The excitation signal was produced by a Tektronix AFG3022C arbitrary function generator and amplified from 10V to 220V using a Krohn-Hite Model 7602M wideband amplifier. The ACT was positioned 3 in. away from the spike surface at an angle of incidence $\alpha = 7.7°$ calculated from the coincidence principle to create a pure AO (acousto-optical) wave mode so that the wave signal focused on a point 1 in. (air gap) from the top surface of the head. The optical sensor (laser Doppler vibrometer) was positioned so that the laser measured the velocity at a point 4.5 in. down the spike from the focus point of the ACT, as shown in Figure 10.

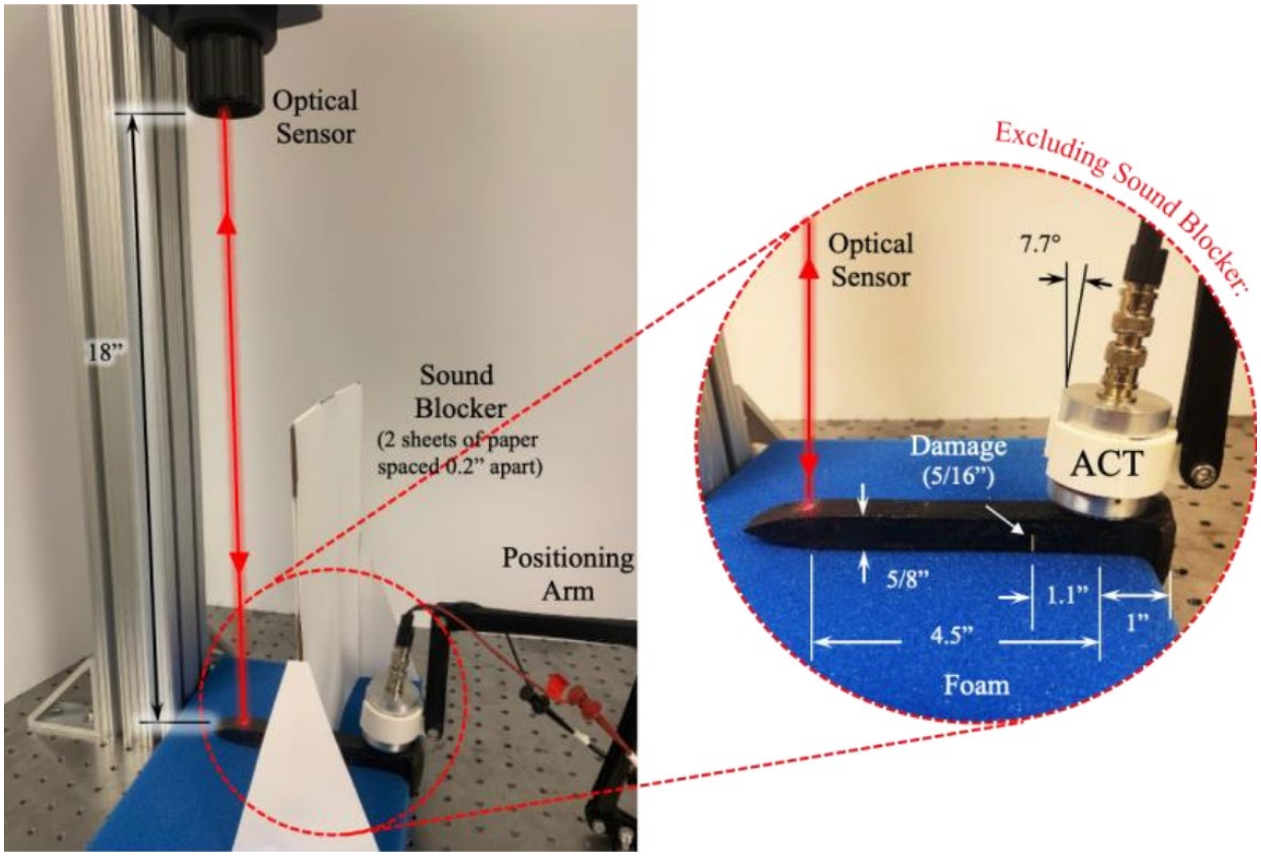

Figure 10. Laboratory Setup with laser and air-coupled transducer at NIA

Figure 11 shows how the ACT emits a pressure wave through the air that generates a guided wave in the steel spike, which is detected through the surface velocity by the optical sensor. This way, any damage present would reflect on the signal, lowering the energy of the wave transmitted through the damage location. Two spikes were tested, one good spike and one spike with a notch cut of 5/16 in. into the spike about 1.5 in. below the spike head.

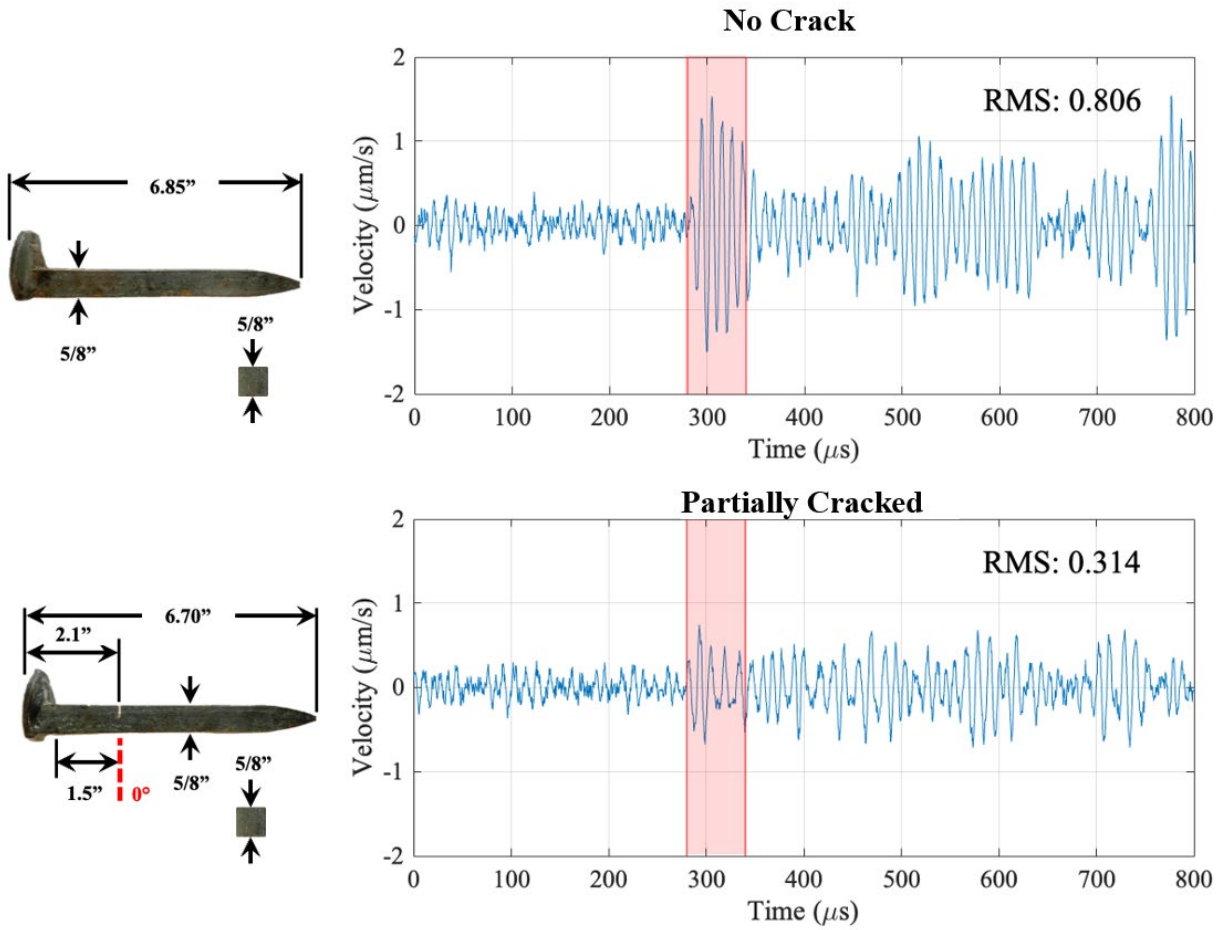


Figure 11. Waveform measured by the optical sensor on the good and partially cracked spikes

From Figure 11, the air-coupled transducer (ACT) emits an ultrasound beam at a certain angle α to select a specific leaky guided (Lamb) A0 wave mode. Note that the coupling from a bulk air wave into the spike was only possible when the wavefront arrived at a certain angle α. The angle α depended on the cross-section of the spike and the combination of the spike material and the surrounding material (air in this laboratory study and wood tie in the field). The guided wave traveled across the damaged spike area, and the signal was received by an optical laser as shown in Figure 10. Results for the experimental setup are presented in Figure 12. For each of the results, the root-mean-squared (RMS) of the amplitude was taken on the time portion of the returned signal where the first received signal was expected. The reduction of RMS magnitude from 0.806 for the good spike case to 0.314 for the partially damaged case indicates that the damage was detectable due to the significant wave amplitude reduction. The effect of the orientation associated with the damage location around the length of the spike was also studied by rotating the spike around its longitudinal axis and measuring the amplitude change of the first received signal. Figure 12 indicates that the first received signal from the good spike has a higher amplitude than the damaged spike at every measured orientation. This suggests that the setup with the air-coupled transducer and optical laser measurement was able to distinguish damaged spikes from spikes without cracks, and the accuracy of the system was not affected by the orientation of the damage, thus proving the volume coverage of the guided waves.

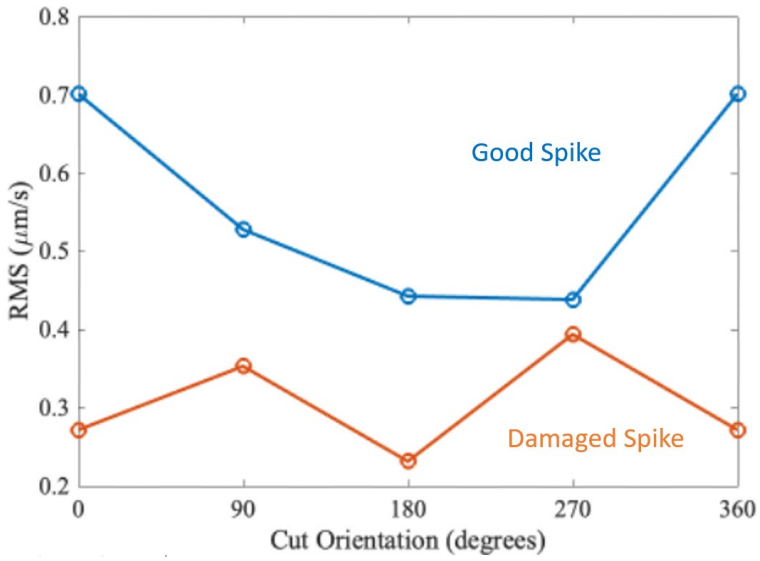


Figure 12. Root mean square (RMS) of the first received signal from the good and damaged spike vs cut orientation.

The test setup presented in Figure 10, and associated results presented in Figures 11 and 12, are based on the spikes laying down on the table, which does not represent the actual spike orientation in the field. Thus, a second experimental setup having a vertical spike was developed to make the experiment condition closer to the realistic scenario. In this setup, the spike is positioned vertically and planted in a column of sand to maintain its position. A similar setup was used before by TTCI to test the ultrasonic approach (Gao et al. 2021). The same signal and instruments were used as the previous setup shown in Figure 10, except the ACT was focused on a point just below the spike head on the shaft region with the square cross-section, and the optical sensor was positioned to measure the velocity on the top of the spike head. This setup is shown in Figure 13.

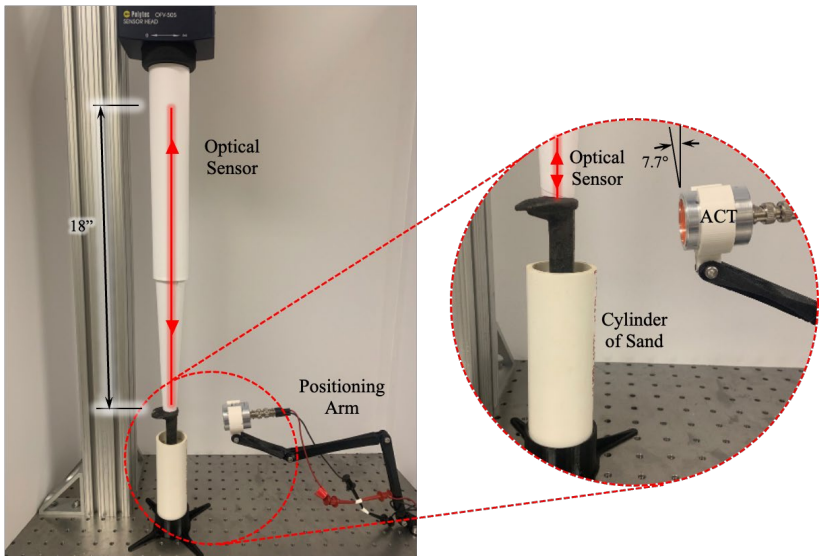


Figure 13. Laboratory Setup with laser and air-coupled transducer and vertical spike at NIA

Results for the vertical spike experimental setup are presented in Figure 14. In each of the presented measured waveforms, the area of time containing the corresponding wave related to different sources is circled. The circle labeled "1" is the result of the signal that is transmitted to the head directly from the focus point of the air coupled transducer. This signal is weak because most of the energy is transmitted down the spike due to the angle. The region labeled "2" is the signal directly from the ACT that has traveled directly through the air to the top of the spike head. The region labeled "3" is the signal that has been reflected from the end of the spike. For the broken spike, this signal arrives much earlier and in a greater magnitude because of the shorter travel distance. Finally, the region labeled "4" for the partially damaged spike is from the reflection at the damage. By comparing the signal between different spikes, we can identify the broken spikes from the partially cracked spike and spike having no crack, due to the higher velocity at the earlier part of the signal.

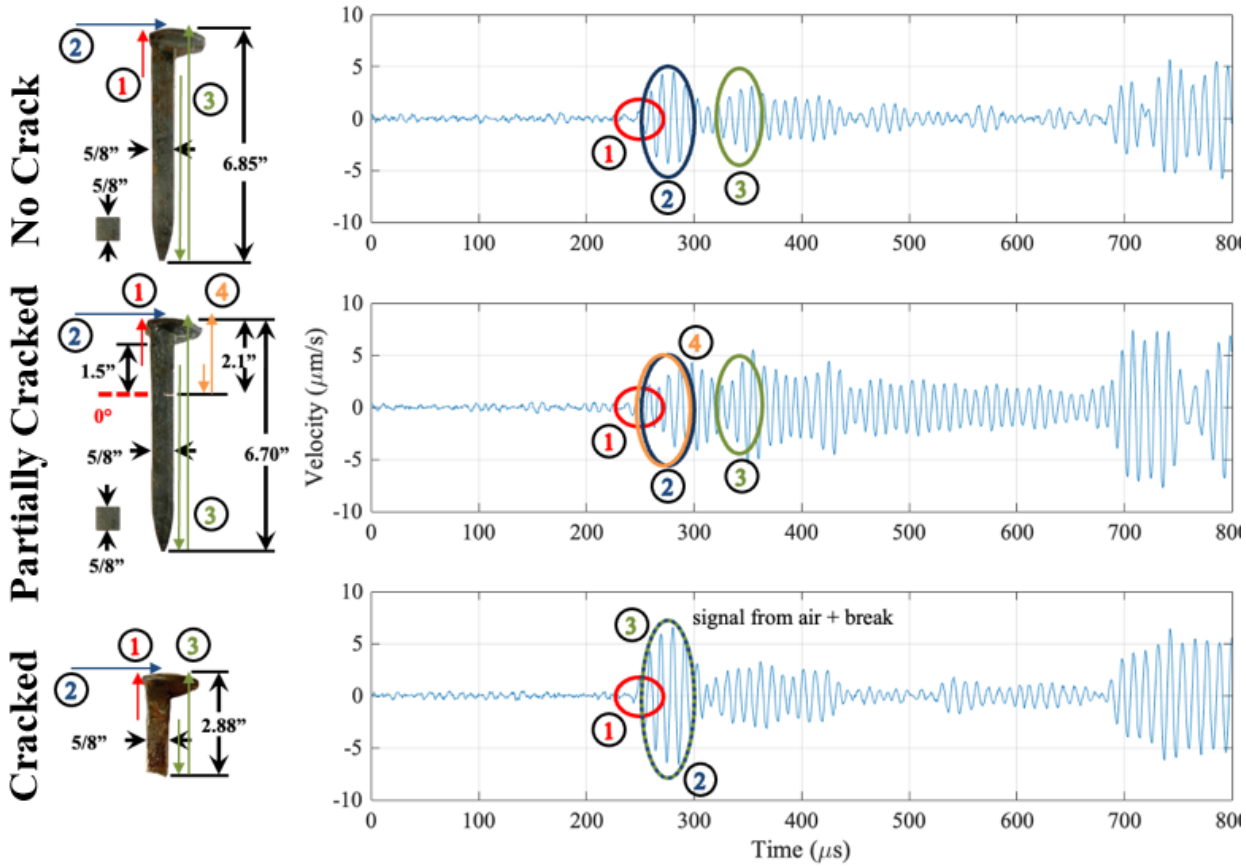


Figure 14. Laboratory Setup with laser and air-coupled transducer and vertical spike at NIA

Similar as Figure 12, Figure 15 shows the root mean square of the signal in the region starting at the first received signal and ending at the conclusion of the signal from the end of the spike. To generate this data, the spike was rotated along its longitudinal axis in increments of 45° to essentially change the orientation of the damage while maintaining itself vertically. It is shown that the damage spike returned a higher amplitude at all angles, indicating that the system is effective for all trials and is not

sensitive to damage orientation. The study again showed the volume coverage of the guided waves.

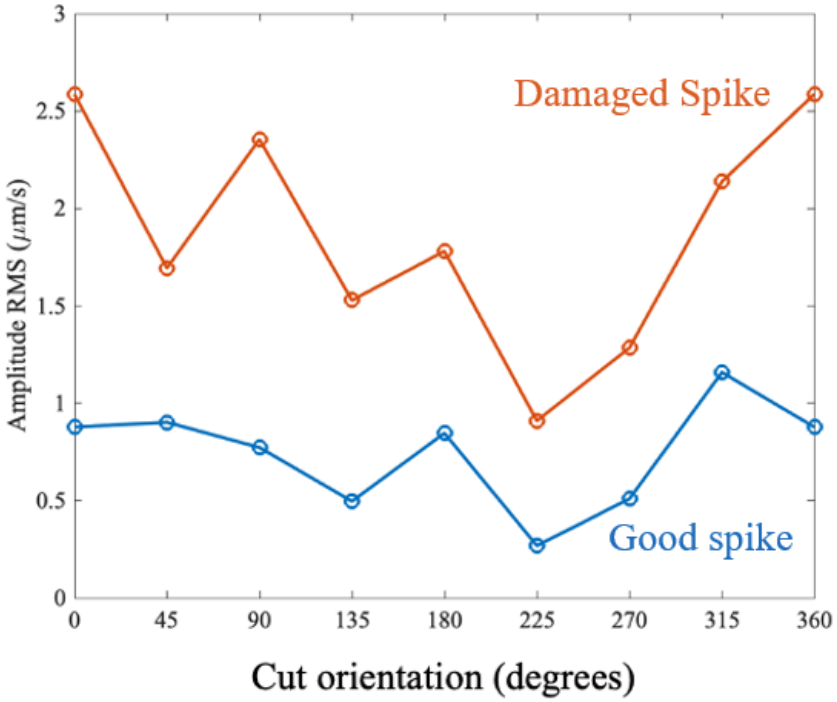


Figure 15. Root mean square (RMS) of the first received signal from the good and damaged spike vs cut orientation.

There are some limitations that should be pointed out. The experiment with the guided wave and air-coupled transducer shows promising results in the well-controlled laboratory environment, indicating this technology may have potential to be further developed and verified in the field performance. However, there are some important factors the laboratory experiments have not considered properly so far, such as: 1) the interactions between the tie and the spike, 2) the interaction between the spike and the tie plate and rail, 3) the spike angle, 4) the crack depth, and 5) different spike materials. The timber tie may have a different restraint to the spike than the sand used in the laboratory experiment, and the influence of the different restrain could cause the signal to be harder to distinguish. The tie plate was also made from steel that was similar to the spike material, and the wave could divert at the interface between the tie plate and the spike. Also, different spikes may not have exactly the same material properties, even though they were all made with steel having similar properties. Also, one cannot assume all the spikes were nailed down perfectly perpendicular to the tie plate. Thus, the input wave as shown in Figures 10 and 13 could be inconsistent in field applications. The actual field performance of the proposed method needs to be verified in the future.

## 3. Automatic Spike Detection

No matter what excitation and measurement methods are used to inspect the spikes, the spikes need to be recognized and located in the field. Without automatic spike recognition and segmentation capability, any proposed spike inspection method will be limited in inspection efficiency due to the need of manually positioning the sensors or excitation source from one spike to another. This project developed an automatic track object recognition and segmentation model that can identify and locate the spikes efficiently in the field.

***Computer vision model development***

To accurately identify multiple railroad track components, YOLACT-Res2Net-50 and YOLACT-Res2Net-101, which adapt a new backbone architecture compared to the original models, are proposed and evaluated in this study. Figure 16 presents the main structure of the proposed models. Specifically, the main structure includes backbone (feature extractor), feature pyramid network (FPN), prediction head (generating anchors), and Protonet (predicting k prototype masks). In general, instance segmentation is more difficult than object detection since it heavily relies on feature localization to generate masks, resulting in low speed and impractical in field applications. Nevertheless, the YOLACT type model separates the instance segmentation into two parallel tasks. One is responsible for generating prototype masks using the Protonet (a fully convolutional network) over the entire image, and the other one focuses on predicting anchors and mask coefficients by using prediction head. These two tasks are assembled by a linear combination, and the outputs are generated with a threshold. In this way, the model improves inference speed and mask quality.

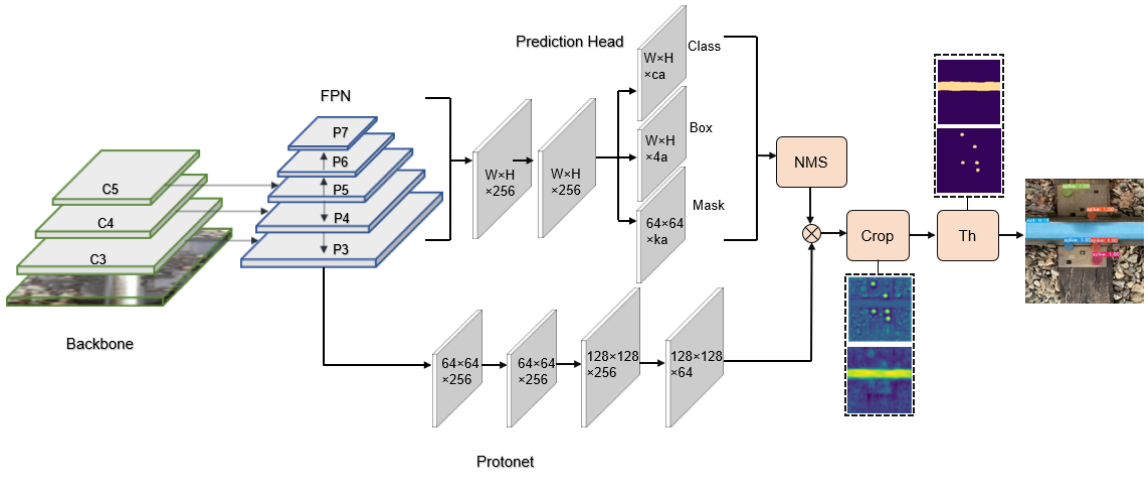


Figure 16. The main structure of the proposed models

In object detection, the backbone acts as the main feature extractor, which takes images or videos as input and yields corresponding feature maps. According to the specific needs of detection accuracy and efficiency, different backbones can be developed for a model after a modification or tuning. For high accuracy, a deep and densely connected backbone, such as the ResNet and DenseNet, can be employed in the model. Considering the speed and efficiency, lightweight backbones, such as the MobileNet and EfficientNet, would be preferred. In this study, to improve the detection

performance, a new backbone, Res2Net, with a stronger multi-scale representation capability, is implemented into the proposed models, YOLACT-Res2Net-50 and YOLACT-Res2Net-101.

Res2Net (Gao et al. 2019) is a new backbone architecture which can improve the multi-scale representation capability at a granular level. Figure 17 shows the architecture of the Res2Net bottleneck which plays an important role in the new backbone. In this bottleneck structure, the original 3×3 filter of n channels shown in Figure 16 is replaced with a set of smaller filter groups. Each group has w channels. Note, n=w×s, where s represents the scale. Note xi is one of the subsets which has 1/s number of channels and the same spatial size with inputs. For each feature subset xi (i ≥2), there is a 3×3 convolution corresponding to it, namely as Ki (). While for x1 and y1=x1, there is no convolution. Each output feature map, yi, is the output of Ki (). During the following model training and evaluation in this study, w is assigned to 26 and s is assigned to 4.

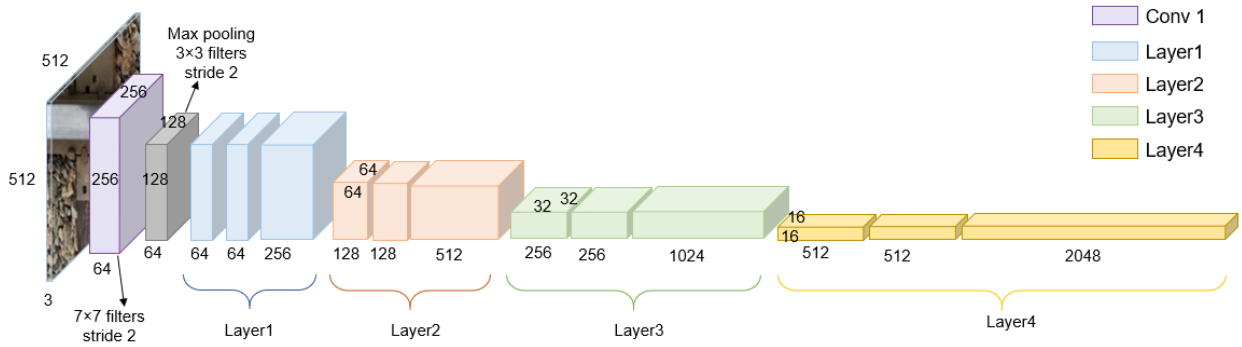


Figure 17. Main structure of ResNet-50

To better show the improved network architecture, Table 1 presents the detailed parameters of the proposed YOLACT-Res2Net-50 backbone. As shown in Figure 16, there are five stages: Conv1, Layer1, Layer2, Layer3, and Layer4. It also can be referred in the filter size shown in Table 1. The original filters are changed from [1×1, 3×3, 1×1] to [1×1, 3×3, 3×3, 3×3, 1×1]. Meanwhile, from ×2 to ×4, there are convolutional processes with each kernel. This way, as the literature (Gao et al., 2019) mentioned, the range of receptive fields for each network layer will increase. Therefore, the model will have better detection performance. Besides, it is worth noting that the introduced feature sets cause changes in the output channels.

To detect objects on multiple scales, Feature Pyramid Network (FPN) (Lin. et al., 2017) has widely been used in many object detection and segmentation models. Typically, the composition of an FPN includes a bottom-up pathway, a top-down pathway, and lateral connections. The bottom-up pathway is the feed-forward computation for the backbone to extract features in the inputs. The assembly of convolution layers with the same output feature size is denoted as the stage in the FPN. Specifically, the backbone, as shown in Figure 16, {C3, C4, C5} is the output of the last residual blocks in the stage of Layer2, Layer3, and Layer4, respectively. When layers go up, the spatial resolution decreases. In terms of the top-down pathway, it constructs the high-resolution layers from higher layers in the pyramid which are semantically strong, but not precise. Hence, the later connections are then used to merge the features from the bottom-up pathway and top-down pathway for a better prediction on the object locations. The original set of feature output in the FPN is {P3, P4, P5}, corresponding to {C3, C4, C5}. In the YOLACT type models, to increase the detection

performance on the small objects, P5 is upsampled to P6 and P7 with one-fourth dimensions; meanwhile, P2 is omitted.

Table 1 The detailed specifications of backbone of proposed Res2Net-50

| *Layer* | *Type* | *Filter size* | *Stride* | *Output channels* | *Output size* |
|---|---|---|---|---|---|
| Input image | | | | | 512 |
| Conv1 | Max pooling | 7×7 | 2 | 64 | 256 |
| | | 3×3 | 2 | 64 | 128 |
| Layer1 | bottleneck | $\begin{bmatrix} 1\times1,\ 104 \\ 3\times3,\ 26 \\ 3\times3,\ 26 \\ 3\times3,\ 26 \\ 1\times1,\ 256 \end{bmatrix}\times3$ | | 256 | 128 |
| Layer2 | bottleneck | $\begin{bmatrix} 1\times1,\ 208 \\ 3\times3,\ 52 \\ 3\times3,\ 52 \\ 3\times3,\ 52 \\ 1\times1,\ 512 \end{bmatrix}\times4$ | | 512 | 64 |
| Layer3 | bottleneck | $\begin{bmatrix} 1\times1,\ 416 \\ 3\times3,\ 104 \\ 3\times3,\ 104 \\ 3\times3,\ 104 \\ 1\times1,\ 1024 \end{bmatrix}\times6$ | | 1024 | 32 |
| Layer4 | bottleneck | $\begin{bmatrix} 1\times1,\ 832 \\ 3\times3,\ 208 \\ 3\times3,\ 208 \\ 3\times3,\ 208 \\ 1\times1,\ 2048 \end{bmatrix}\times3$ | | 2048 | 16 |

To improve the operation speed, instance segmentation is achieved by two parallel tasks in the original and improved models. One of the parallel tasks, generating prototype masks, is completed by Protonet. It is worth noting Protonet is a fully connected network (FCN) which is attached to the P3 layer in the FPN. The architecture of Protonet can be seen in Figure 16. In this branch, k Protonet masks without loss computations are proposed for the entire image. To improve the instance segmentation performance, we increase the k from 32 to 64 in the proposed models. A nonlinear activation function, ReLU, is used to keep the outputs from Protonet unbounded and generate more interpretable prototypes. It also needs to mention that the number of prototype masks are independent of the number of categories; thus, it can lead to a distributed representation for the generated prototypes. Example prototype images generated by the proposed YOLACT-Res2Net-50 are shown in Figure 18. The high-resolution prototypes are beneficial for mask quality and detection performance on small objects.

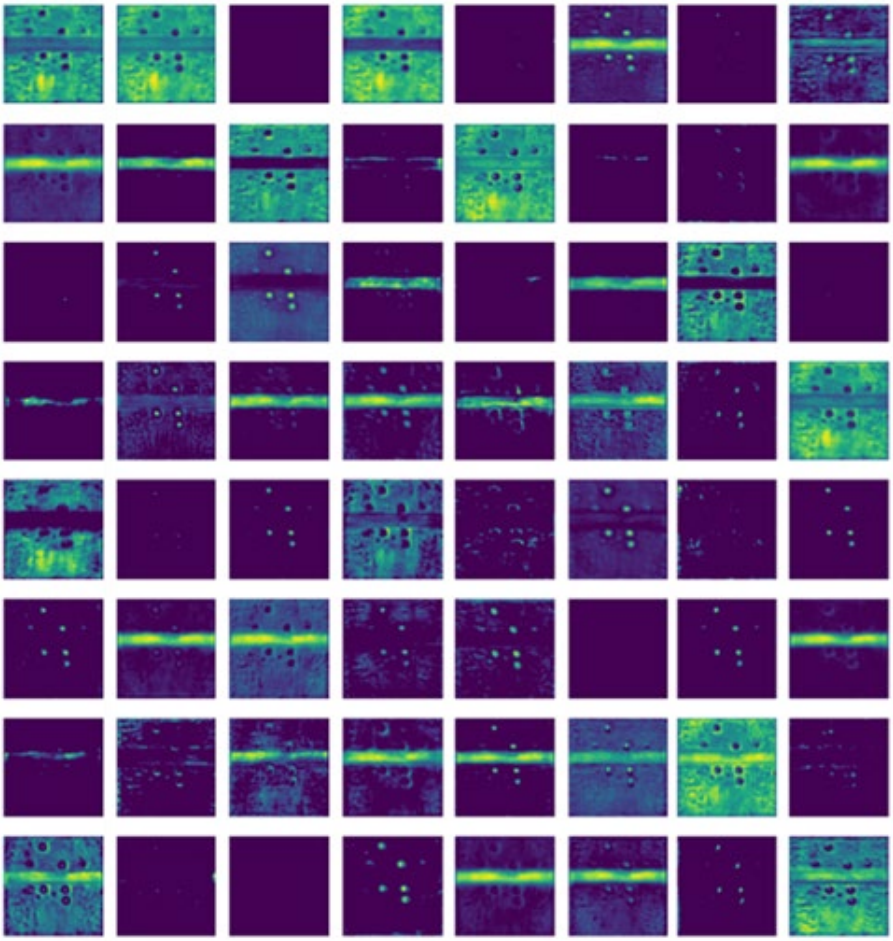

Figure 18. Prototype image generation

***Detection performance evaluation***

To validate the performance of the proposed models and compare them with the original models having their default backbones, five models are trained and tested in this study. Specifically, the original models are YOLACT-ResNet-50 and YOLACT-ResNet-101. The improved models are named as YOLACT-Res2Net-50 and YOLACT-Res2Net-101. In addition, Mask R-CNN, which represents the high mask quality and the high accuracy on object detection, is trained and evaluated, aiming to improve the comparison between Mask R-CNN and the improved models. For the original models and the improved models, the training processes are completed in the same module. For Mask R-CNN, MMDetection (Chen et al., 2019) which is an open-source object detection toolbox based on Pytorch, is adopted for friendly usage, training, and evaluation. The detection results generated from different models are evaluated based on MS COCO evaluation metric (Lin et al., 2014) aiming to compare the results fairly and comprehensively. The validation curves generated from the training and validation process of the original and improved models are plotted and discussed. For Mask R-CNN, since there are differences between different training modules, only AP, AP50, and AP75 are compared and evaluated in Table 2.

The images are saved from video frames recorded on an iPhone® 8 smartphone with a 12-megapixel main camera, of which has a single wide-angle lens with an f/1.8 aperture. The videos are taken from

a railroad section beside 300 Main St. Columbia, SC. The section is between GPS coordinates [33.988208, -81.025973] and [33.989474, -81.025942]. The smartphone is held in hand and the video is taken at a walking speed along the track. A total of 30 minutes of video is recorded and saved on the smartphone. The original video resolution is 1920×1080, and the converted image size is set to 512×512 to meet the training image size requirement. Three types of rail components, including rail, spike, and clip, are included in the image database. To prevent overfitting, the training images are processed with image augmentation, including mirroring, rotation (90°), and the combination of rotation (180°) and gaussian noise. A popular labeling tool, labelme (Wada, 2016) is employed to generate the annotation files.

The output JSON files are converted to COCO format based on the prepared code for training, validation, and evaluation. Figure 19 shows the ground truth and the labeling mask. To reduce the bias and ensure the training processes are statistically significant, the 5-fold cross-validation is performed in the training procedure. Specifically, 1000 images are randomly split into 5 folds, and each fold contains 200 images. Each group is taken as a test set, and the remaining groups are considered as the training set. In total, 25 training and tests are for the entire dataset. The evaluation results, including the mean values and standard deviations, are shown in Table 2.

Figure 19. Example of original jpg image and label result (a) Ground truth (b) instance label visualization

Table 2 COCO mAP results with different models in this study on custom dataset.

| | Method | AP | SD | $AP_{50}$ | SD | $AP_{75}$ | SD |
|---|---|---|---|---|---|---|---|
| bbox | YOLACT-Res2Net-50 | 59.4 | 2.4 | 97.7 | 1.6 | 65.6 | 6.2 |
| | YOLACT-Res2Net-101 | 59.9 | 2.2 | 97.9 | 1.2 | 67.3 | 5.2 |
| | YOLACT-ResNet-50 | 56.4 | 1.8 | 97.1 | 1.4 | 59.8 | 5.1 |
| | YOLACT-ResNet-101 | 57.4 | 1.9 | 97.1 | 1.9 | 60.3 | 3.9 |
| | Mask R-CNN | 63.9 | 3.4 | 97.6 | 1.5 | 76.6 | 7.7 |
| mask | YOLACT-Res2Net-50 | 63.2 | 7.3 | 97.3 | 1.7 | 69.7 | 12.8 |
| | YOLACT-Res2Net-101 | 63.6 | 6.8 | 97.3 | 1.9 | 64.4 | 12.7 |
| | YOLACT-ResNet-50 | 59.6 | 6.6 | 96.5 | 1.8 | 66.5 | 12.0 |
| | YOLACT-ResNet-101 | 61.0 | 6.9 | 96.5 | 2.5 | 68.3 | 12.3 |
| | Mask R-CNN | 61.6 | 6.6 | 97.2 | 1.6 | 64.4 | 12.7 |

*Note: AP50 is AP @ IoU = 0.5; AP75 is AP @ IoU = 0.75; SD is standard deviation.*

Based on these results, it is reasonable to believe the improved models outperform the original models. To evaluate the detection performance on a wider scale, the MS COCO evaluation matric

with AP50 and AP75 are performed and shown in Table 2. It shows that the proposed models, YOLACT-Res2Net-50 and YOLACT-Res2Net-101, have competitive performance in the detection of bounding boxes and masks. For detecting bounding boxes, considering the AP values, the proposed models outperform the original models by 3 AP and 2.5 AP, respectively, while Mask R-CNN achieves the highest AP value, 63.9. With a 50% IoU threshold, there is not much difference in AP values between different models, while the improved models perform better when the IoU threshold is 75%. The proposed models outperform the original models by 5.8 AP and 7 AP, respectively. Meanwhile, Mask R-CNN has the highest AP value, 76.7. Regarding the standard deviation (SD), all the models have low SD values with different training and testing sets, indicating the bounding box prediction results are solid, reliable, and statistically significant. The improved models are more effective on the bounding box prediction compared to the original ones.

In terms of the instance segmentation performance, the proposed models are able to improve the mask accuracy compared to the original models and Mask R-CNN. For the AP values, YOLACT-Res2Net-101 has the highest mask AP value, which is 2.6 higher than the value of the original one. YOLACT-Res2Net-50 improves AP by 4 compared to its original model. Regarding the performance of instance segmentation with an IoU threshold of 50%, the proposed models both achieve AP50 of 97.3, which are higher than the values of the original models and Mask R-CNN. When the IoU threshold is 75%, YOLACT-Res2Net-50 achieves the AP75 of 69.7, which is 3.2 higher compared to the value of its original model. The proposed YOLACT-Res2Net-101 model has a lower AP75 value, which is 3.9 lower compared to its original model. Since the AP value computation needs different thresholds, although the proposed model performs a bit worse with one of the thresholds, overall, it still performs very well. For the SD values on mask detection, it can be found that they are lower on the AP50 but are higher on the AP75. This needs to be considered for future improvement.

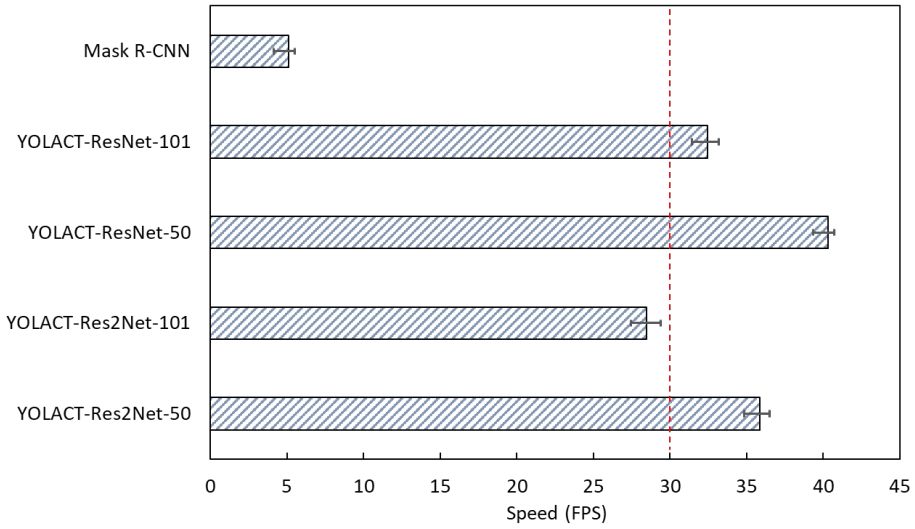

Figure 20. Detection speed of different models

The detection strategy of Mask R-CNN is to propose lots of candidate proposals, so Mask R-CNN performs better on the bounding box, and it has been proved to be effective as shown in Table 2.

However, as a trade-off, from Figure 20 it can be seen the detection speed of Mask R-CNN is much lower compared to YOLACT models. The average inference speed of Mask R-CNN is 5.3 FPS with a standard deviation of 0.36, while the original and improved models inference time is close to or over 30 FPS, indicating a possible real-time application in the field inspection. The inference speeds of the proposed YOLACT-Res2Net-50 and YOLACT-Res2Net-101 models are 35.9 FPS (SD=0.65) and 28.4 FPS (SD=0.92), respectively. They are slightly slower compared to the original models which have 40.3 FPS (SD=0.40) and 32.4 FPS (SD=0.76). The possible reason could be that more receptive fields cost more computational power, and this leads to potential optimization research in the future. In short, the proposed YOLACT-Res2Net-50 performs the best on bounding box detection in a real-time speed, and YOLACT-Res2Net-101 has the best mask accuracy.

***Detection performance with different illumination conditions***

In the field practice, environmental conditions are complex, and the track components are relatively small, making visual inspections very challenging. Besides, the inspection window has been reduced due to the busier timetables. Therefore, any detection model has to be robust enough to accommodate harsh environmental conditions for field applications. One of the typical challenges in the field is the light condition. To test the detection performance under different light conditions, five different light intensities are used on the 24-bit depth images, which are original light, light-10%, light-30%, light-50%, and light-70%. Figure 21 shows the testing results under the selected five visibility conditions.

Looking at the ground truth with naked eyes, there are obvious differences between the normal and dimmed conditions. As the light decreases, the image background becomes darker, and the rail components are blended into the background. It is indeed challenging to distinguish the rail components by naked eyes without sufficient light as shown in the first row in Figure 21. Furthermore, the specific image presented in Figure 21 is taken during a rain, making it more troublesome for detection. For the track segment where the images are taken, each tie plate has five spike holes, three on the field size and two on the gauge side. Two spike holes on each side are with spikes. In the image in Figure 21, there are five visible spikes, one rail, and four clips. The spikes on the gauge side area are easily seen, but only one spike can be seen on the fire side, with the other three on the gauge side being blocked by ballast or leaves. The results of the detection accuracy of each model under different light conditions are presented in Figure 22. For YOLACT-ResNet-50, in the first four light conditions, it successfully detects all the spikes and the clips. However, it cannot detect the rail and add a mask on it. In the darkest condition, light-70%, it missed two spikes. YOLACT-ResNet-101 is similar to YOLACT-ResNet-50. It also fails to detect the rail; meanwhile, it misses three spikes under the light-70% condition. Regarding the proposed YOLACT-Res2Net-50, except for the last condition, it successfully detects the rails and adds the masks on them. Under the light-70% condition, it misses one spike. The proposed YOLACT-Res2Net-101 also performs well under each condition. It detects the rails and adds mask on them under four different light conditions, but it misses three spikes in the darkest condition. It is worth noting that the last model, Mask R-CNN has good performance in different light conditions. It detects three rails out of all rails. Meanwhile, it just misses two spikes in the darkest condition.

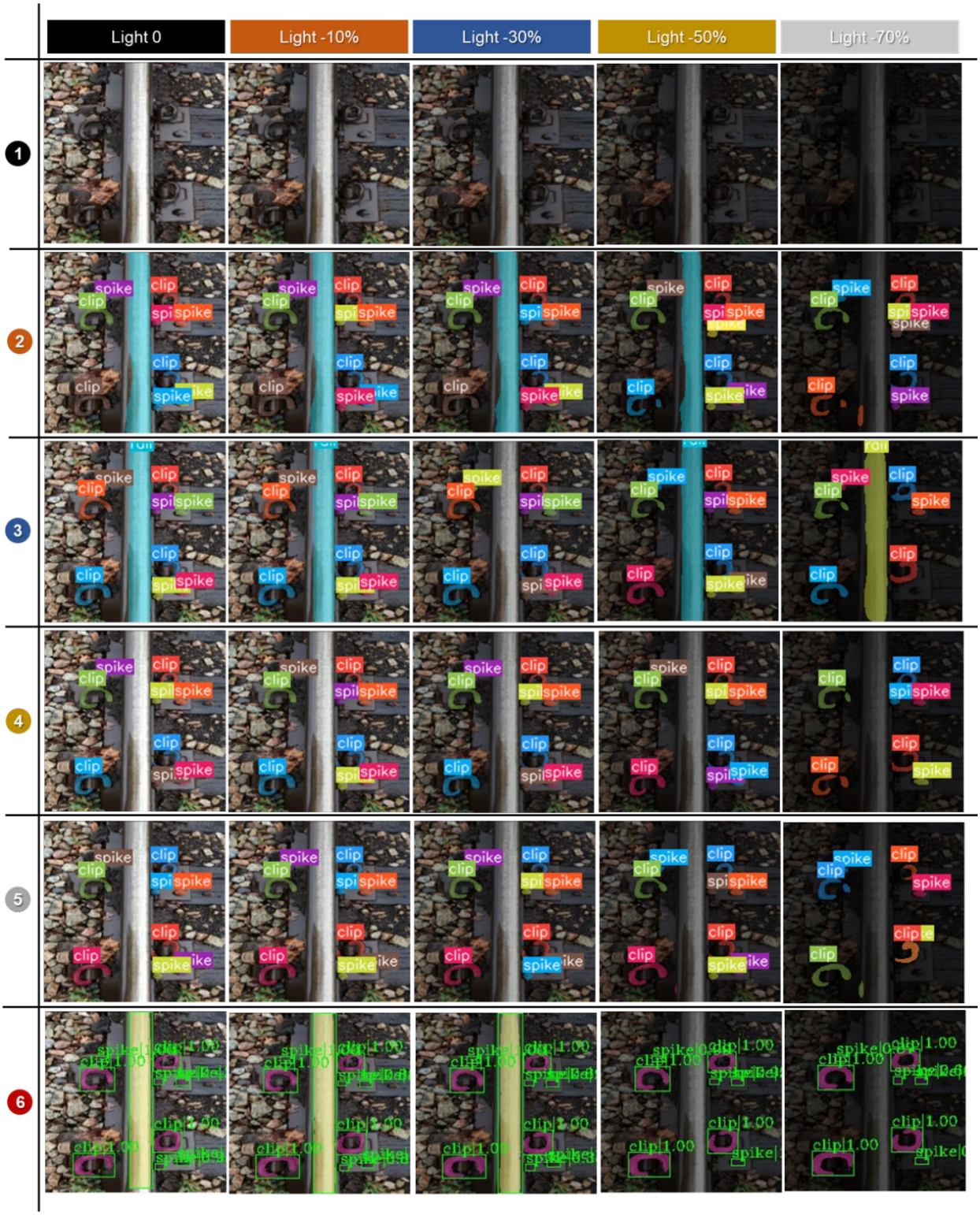


Figure 21 Representative detection results on the different light condition 1: Ground truth; 2: YOLACT-Res2Net-50; 3: YOLACT-Res2Net-101; 4: YOLACT-ResNet-50; 5: YOLACT-ResNet-101; 6: Mask R-CNN

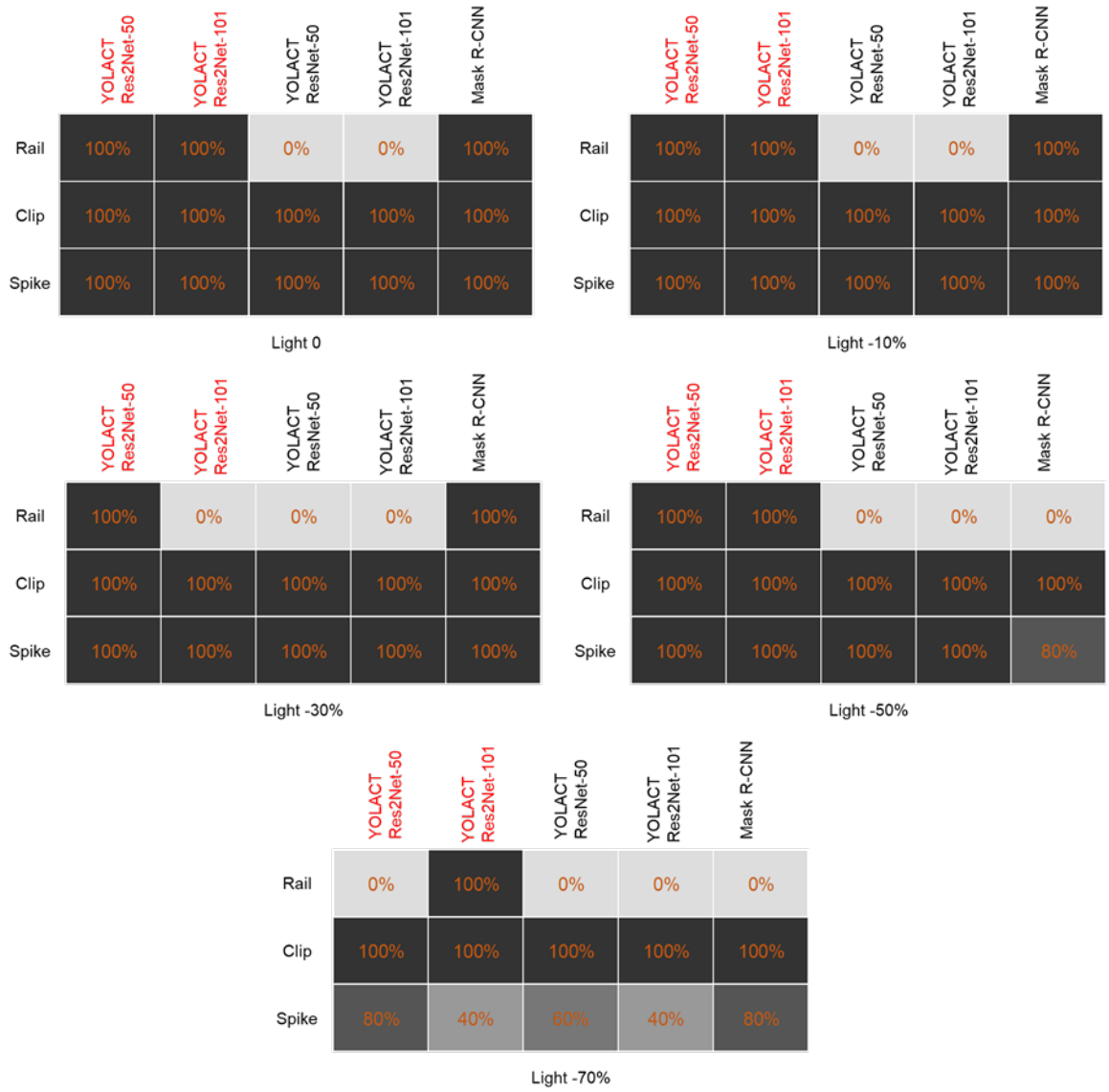


Figure 22 Detection accuracy under different illuminations.

Overall, our improved models outperform the original models and Mask R-CNN under five lighting conditions. It should be mentioned that the test image is randomly selected from the image set. To some extent, it can reflect the real performance in the field practice. Currently, limited by the training data, other types of track components are not included. In the future, the detection performance can be improved with more data and further enhancement of the model.

## Concluding Remarks

In this project, both the numerical parametric analysis and laboratory experiment have been conducted to explore a potential solution to distinguish damaged spikes from good spikes in a non-contact fashion with the assistance of laser and corresponding sensors. With the results obtained so far, the following concluding remarks can be drawn:

(1). With proper excitation, damaged spikes and good spikes would generate different signals due to different wave propagation patterns within the spike shafts.

(2). Using direct laser excitation does not appear to be a good solution because the high reflection properties of the spike material. Most of the laser energy would be scattered and cause safety concerns. The small portion of the absorbed laser energy could not produce meaningful signals. It is hard to directly measure any meaningful results with ordinary microphones.

(3). Using the guided wave method, air-coupled transducer and optical laser setup has great potential to distinguish the damaged spike from the good spikes. The first received signal from the good spike has a higher amplitude than the damaged spike which can be served as a criterion. Both experiments with horizontally and vertically oriented spikes showed promising performance. The air-coupled transducer is also able to detect the partially cracked spikes in the well-controlled laboratory environment.

(4). An improved real-time instance segmentation model for automatic railroad track component detection is developed based on a fully convolutional model which includes backbone, FPN, Protonet, and prediction head. This model is able to perform real-time (inference speed >30 FPS) spike instance segmentation with high accuracy on a single GPU. Under the different light conditions, our proposed models outperform the other models, proving the robustness on low visibility conditions.

# References


1. American Railway Engineering and Maintenance-of-Way Association. Manual for railway engineering. Lanham, Maryland: AREMA; 2014.
2. Chen, K., Wang, J., Pang, J., Cao, Y., Xiong, Y., Li, X., Xu, J. (2019). MMDetection: Open mmlab detection toolbox and benchmark. arXiv preprint arXiv:1906.07155.
3. Dersch, M. S., Roadcap, T, Edwards, J. R., Qian, Y., Kim, J. Y., and Trizotto, M. "Investigation into the Effect of Lateral and Longitudinal Loads on Railroad Spike Stress Magnitude and Location using Finite Element Analysis," Engineering Failure Analysis, Vol. 104, pp. 388-398, 2019.
4. Dersch, M. S., Silva, M. T., Edwards, J. R., de O. Lima, A., and Roadcap, T. "Analytical Method to Estimate Railroad Spike Fastener Stress," Transportation Research Record, Vol. 2674, No. 11, pp. 379-389, 2020.
5. Dersch, M.S., Khachaturian, C.J. and J.R. Edwards. 2021. Methods to mitigate railway premium fastening system spike fatigue failures using finite element analysis. Engineering Failure Analysis. 121 (March 2021): 105160. doi:10.1016/j.engfailanal.2020.105160.
6. Dersch, M.S., M. Trizotto Silva, J.R. Edwards and A. de O. Lima. 2021. Quantification of vertical, lateral, and longitudinal fastener demand in broken spike track: Inputs to mechanistic-empirical design. Journal of Rail and Rapid Transit. 1-13. doi:10.1177/09544097211030736.
7. Gao, S., Cheng, M.-M., Zhao, K., Zhang, X.-Y., Yang, M.-H., & Torr, P. H. (2019). Res2net: A new multi-scale backbone architecture. IEEE transactions on pattern analysis and machine intelligence.
8. Gao, Y., McHenry., M., and Kerchof, B. "Investigation of Broken Cut Spikes on Elastic Fastener Tie Plates using an Integrated Simulation method," 2018 Joint Rail Conference. American Society of Mechanical Engineers Digital Collection, 2018.
9. Gao, Y., Poudel, A., and Lindeman, B., "Automated Broken Spike Detection–Phase I," No. DOT/FRA/ORD-21/17," United States. Federal Railroad Administration. Office of Railroad Policy and Development, April 2021.
10. Kerchof, B., "A Derailment Investigation and Broken Spikes," WRI 2017, Presentation at the 2017 Wheel Rail Interaction Conference, Montréal, Canada. 2017.
11. Kunz, A., and Wegener, K. (2010). "Evaluation of reflectivity of metal parts by a thermo-camera", Proceedings of InfraMation 2010, November 8-12, 2010 Las Vegas
12. Harb, M.S., Yuan, FG. Air-Coupled Nondestructive Evaluation Dissected. J Nondestruct Eval 37, 50 (2018). https://doi.org/10.1007/s10921-018-0502-4
13. Lin, T.-Y., Dollár, P., Girshick, R., He, K., Hariharan, B., & Belongie, S. (2017). Feature pyramid networks for object detection. Paper presented at the Proceedings of the IEEE conference on computer vision and pattern recognition.
14. Lin, T.-Y., Maire, M., Belongie, S., Hays, J., Perona, P., Ramanan, D., Zitnick, C. L. (2014). Microsoft coco: Common objects in context. Paper presented at the European conference on computer vision.
15. Roadcap, T., Dersch, M., & Edwards, J. R., "Mechanistic Investigation of Timber Crosstie Spike Failures," Transportation Research Board Annual Meeting 2019, Washington, DC. 2019.
16. Setiawan, A., Suparta, G.B., Mitrayana, L., and Nugroho, W. (2018). "Surface Crack Detection with Low-cost Photoacoustic Imaging System." International Journal of Technology 9(1)
17. Stuart, C., Dersch, M. S. and Edwards, J. R. "Timber Crosstie Spike Fastener Failure Investigation: Field Evaluation of an Alternative Fastener [Research Results]," No. RR 20-24. United States. Department of
18. Stuart, C., Roadcap, T., and Dersch, M. S. "Timber Crosstie Spike Fastener Failure Investigation," No. RR 19-14. United States. Federal Railroad Administration. Office of Research, Development & Technology, 2019.
19. Transportation. Federal Railroad Administration. Office of Research, Development, and Technology, 2020.
20. Trizotto, M., Dersch, M., Roadcap, T., Edwards, J. R., & Lima, A. "Mechanistic Investigation of Timber Crosstie Spike Failures," Preliminary Findings from the Laboratory and Field, Tucson, AZ. 2019.
21. Wada, K. (2016). labelme: Image Polygonal Annotation with Python.
22. Yu, H., and Liu, S. "Finite Element Analysis of Spike Failure in Elastic Fastening Systems for Wood Ties," 2019 Joint Rail Conference. American Society of Mechanical Engineers Digital Collection, 2019.

# Appendix: Research Results

**What was the need?**

Although many new types of elastic fasteners and concrete ties have been recently introduced, spikes, together with tie plates, are still one the major fastening systems in North American freight railroads. With the increasing axle load and operational speed, spikes are subjected to more demanding loading conditions, especially in the territories where tracks have high curvature (Dersch et al. 2019, Roadcap et al, 2019, Trizotto et al. 2019, Dersch et al. 2020). It is reported that broken spikes were frequently observed, including cut spikes, screw spikes, and driven spikes that were used to restrict both tie plates and rails (Gao et al. 2018, Roadcap et al, 2019). Since cracks typically develop between one and two inches below the top of the tie, it is very difficult to distinguish the broken spikes without physical examination, which causes formidable challenges in track health evaluation and operational safety (Gao et al. 2018, Roadcap et al, 2019). Several recent derailments in Canada and the United States are attributed to a large number of broken spikes or screws within a certain section of track (Kerchof 2017). A recent investigation conducted by Roadcap et al. (2019) identified at least 11 derailments were due to the broken spikes. Thus, it is in urgent need to study on feasible yet practical solutions of railroad spike inspection.

**What was our goal?**

Considering the enormous number (estimated around two billion) of spikes in service in North America, the drastic consequences of unrecognized broken spikes, and the challenge to quantify the service condition of the spikes, our goal is to develop a non-destructive and contact-free intelligent inspection system that can be deployed for track inspections. We aim to develop the laser-based, non-destructive spike defect inspection system based on laser excitation, acoustic analysis, computer vision and pattern recognition, and artificial intelligence (AI).

**What did we do?**

A numerical model of a spike based on the finite element method was established to simulate the heat transfer from laser excitation and corresponding thermal expansion and wave propagation within the spike. Three different types of spikes, good spike (new spike with no crack), partially cracked spike, and completely broken spike, are included in the model. Laser excitation was simulated as a heat source at the spike head area to mimic different laser exposure times and focus areas. The wave caused by the laser excitation at the spike head area can be reproduced by the numerical model to present the wave initiation and propagation within the spike.

A series of laboratory experiments were performed with the guidance from the numerical simulation results. Different spikes were excited with a laser directly hit at the spike head at different laser intensities. Both a microphone and air-coupled transducer were used to detect the reflection waves away from the spike in a non-contact fashion to distinguish any difference that may show between the signals from good spikes and broken spikes. The specific laboratory setup with the air-coupled transducer developed in this project could pick up the differences between the signals from good spikes and broken spikes.

A real-time pixel-level detection framework with improved real-time instance segmentation models is developed based on a fully convolutional model including backbone, FPN, Protonet, and prediction head. The developed algorithm leverages fast object detection and highly accurate instance segmentation. Track components such as spike, clip, and rail can be detected in real-time (inference speed over 30 FPS) with a single GPU.

**What was the outcome?**

The experimental result in this study indicates that if using an ordinary microphone, the laser needs to have high power; however, it may cause laser scattering issues due to the high reflective properties of the spike head surface. Thus, it is not feasible to use ordinary microphone for broken spike detection purpose. On the other side, with an ultrasonic guided wave and air-coupled transducer, it can distinguish the broken spike from good spike in the laboratory setup, which provides a feasible solution for broken spike detection. The computer vision model developed in this study is able to detect spike and other track components and shows robust performance on low visibility conditions. The automatic spike recognition algorithm could assist rapid spike inspection in the field.

**What is the benefit?**

With the developed computer vision model and the non-destructive inspection approach, it is possible to further develop a field-deployable system that can perform rapid spike inspection to distinguish broken spikes. Quantifying the broken spikes efficiently could improve railroad track safety and assist with better track maintenance planning.